A Study of Multiple Tropopause Structures Caused by Inertia–Gravity Waves in the Antarctic

RYOSUKE SHIBUYA AND KAORU SATO

Department of Earth and Planetary Science, University of Tokyo, Tokyo, Japan

YOSHIHIRO TOMIKAWA AND MASAKI TSUTSUMI

National Institute of Polar Research, and Graduate University for Advanced Studies (SOKENDAI), Tokyo, Japan

TORU SATO

Department of Communications and Computer Engineering, Kyoto University, Kyoto, Japan

(Manuscript received 30 July 2014, in final form 15 November 2014)

ABSTRACT

Multiple tropopauses (MTs) defined by the World Meteorological Organization are frequently detected from autumn to spring at Syowa Station (69.0°S, 39.6°E). The dynamical mechanism of MT events was examined by observations of the first mesosphere–stratosphere–troposphere (MST) radar in the Antarctic, the Program of the Antarctic Syowa MST/Incoherent Scatter (IS) Radar (PANSY), and of radiosondes on 8–11 April 2013.

The MT structure above the first tropopause is composed of strong temperature fluctuations. By a detailed analysis of observed three-dimensional wind and temperature fluctuation components, it is shown that the phase and amplitude relations between these components are consistent with the theoretical characteristics of linear inertia–gravity waves (IGWs).

Numerical simulations were performed by using a nonhydrostatic model. The simulated MT structures and IGW parameters agree well with the observation. In the analysis using the numerical simulation data, it is seen that IGWs were generated around 65°S, 15°E and around 70°S, 15°E, propagated eastward, and reached the region above Syowa Station when the MT event was observed. These IGWs were likely radiated spontaneously from the upper-tropospheric flow around 65°S, 15°E and were forced by strong southerly surface winds over steep topography (70°S, 15°E). The MT occurrence is attributable to strong IGWs and the low mean static stability in the polar winter lower stratosphere.

It is also shown that nonorographic gravity waves associated with the tropopause folding event contribute to 40% of the momentum fluxes, as shown by a gravity wave–resolving general circulation model in the lower stratosphere around 65°S. This result indicates that they are one of the key components for solving the cold-bias problem found in most climate models.

1. Introduction

The tropopause is the boundary between the troposphere and the stratosphere. In 1957, the World Meteorological Organization (WMO 1957) defined the first thermal tropopause as "the lowest level at which the lapse rate decreases to 2°C km^{-1} or less, provided also the averaged lapse rate between this level and all higher levels within 2 km does not exceed 2°C km^{-1}." In addition, the WMO (1957) gives the following definition of the second and additional tropopauses: "If above the first tropopause the average lapse rate between any level and all higher levels within 1 km exceeds 3°C km^{-1}, then a second tropopause is defined by the same criterion as above. This tropopause may be either within or above the 1-km layer." The WMO thermal definition is commonly and operationally used for data obtained from the global upper-air observation network. Using this definition, we can detect a multiple tropopause structure in a single sounding. However, the tropopause can be characterized by several other criteria (Hoskins et al. 1985; Tomikawa et al. 2009). For example, it has been

Corresponding author address: Ryosuke Shibuya, University of Tokyo, 7-3-1 Hongo, Bunkyo-ku, Tokyo 113-0033, Japan.
E-mail: shibuya@eps.s.u-tokyo.ac.jp

DOI: 10.1175/JAS-D-14-0228.1

recognized that the tropopause acts as a boundary of the transport of minor constituents, such as water vapor and ozone (e.g., Gettelman et al. 2011).

Recently, climatology of multiple tropopause (MT) events has been studied by using GPS radio occultation, radiosondes, and reanalysis data (Schmidt et al. 2006; Randel et al. 2007; Añel et al. 2008). Multiple tropopause events are most frequently observed around the subtropical jet over the midlatitudes during winter (Añel et al. 2008). Although a tropopause folding is one of the plausible processes that cause multiple tropopauses in the midlatitudes (Keyser and Shapiro 1986; Danielsen et al. 1991; Lamarque et al. 1996; Koch et al. 2005), multiple tropopause static behavior are somewhat different from tropopause folding behavior (Randel et al. 2007). They showed that spatial patterns of multiple tropopause occurrence frequency do not show maxima in the storm-track region, where those of the tropopause folding occurrence frequency exhibit clear maxima.

The dynamical mechanisms of multiple tropopause structures in the midlatitudes have been closely examined. Randel et al. (2007) suggested that these multiple tropopauses are mainly associated with a tropopause break around the subtropical jet. The tropopause break leads to the tropical tropopause extending to higher latitudes, overlying the lower-stratospheric air. They also showed that when multiple tropopauses are observed, the ozone mixing ratio is smaller over the first tropopause than it is for a single tropopause. The multiple tropopause structures are associated with the poleward transport of tropical tropospheric air above the subtropical jet core. This poleward transport can be attributed to secondary circulation (e.g., Keyser and Shapiro 1986) and tropospheric intrusions, which are both reversible and irreversible (Haynes and Shuckburgh 2000; Berthet et al. 2007; Olsen et al. 2008, 2010; Vogel et al. 2011; Peevey et al. 2014). The tropospheric air intrusion sometimes reaches about 60°N in association with Rossby wave breaking (Pan et al. 2009). Thus, multiple tropopause structures in the midlatitudes are closely related to the stratosphere–troposphere exchange (STE; e.g., Gettelman et al. 2011). Añel et al. (2008) showed that the multiple tropopause structures are also frequently observed in the high-latitude region during winter. However, the dynamics and the characteristics of multiple tropopauses in the polar region have not been closely studied.

Recently, mesosphere–stratosphere–troposphere (MST) radar, which is VHF clear-air Doppler radar, was installed in the Antarctic and began continuous observation on 30 April 2012 at Syowa Station (69.1°S, 39.6°E) [Program of the Antarctic Syowa MST/Incoherent Scatter (IS) Radar (PANSY; Sato et al. 2014)]. This radar provides vertical profiles of three-dimensional winds with fine time and height resolution. It was shown that from autumn to spring, multiple tropopause structures frequently appear, and their time evolution is clearly observed in the echo power of the vertical beam (Sato et al. 2014). We focus on the autumn period from 1 April to 16 May 2013, when multiple tropopauses were observed five times at Syowa Station, to elucidate the dynamics of multiple tropopause structures in the polar region by using the new observational instrument, PANSY. In particular, we discuss the relation of the MTs with inertia–gravity waves (IGWs).

Geller et al. (2013) compared gravity wave absolute momentum fluxes estimated by the data from high-resolution satellite, isopycnic balloon, and high-resolution radiosonde observations, as well as climate models having parameterized gravity waves and gravity wave–resolving general circulation models. Observations and gravity wave–resolving models show that absolute momentum fluxes have a strong peak around the latitude of 60° in the winter stratosphere. Gravity waves in the polar region are important for ozone chemistry (Shibata et al. 2003; Kohma and Sato 2011). Gravity waves are also considered to be a key component to solve the so-called cold-pole bias of most chemistry–climate models for the polar winter stratosphere (Eyring et al. 2010). The cold-pole bias is related to several problems: one of the problems in chemistry–climate model simulations is a significant delay in the breakdown of the stratospheric polar vortex in the Antarctic (Stolarski et al. 2006). Therefore, this bias can result in inaccurate predictions of ozone distributions and their chemical responses in the Antarctic lower stratosphere. McLandress et al. (2012) suggested that the bias is attributable to a shortage of parameterized gravity wave drag around 60°S. Such an underestimation essentially originates from uncertainties in both orographic and nonorographic gravity wave parameterizations. Interestingly, Geller et al. (2011) found it necessary to have greater nonorographic gravity wave sources in Southern Hemisphere winter high latitudes than at Northern Hemisphere winter high latitudes to eliminate wind and temperature biases in their version of the Goddard Institute for Space Studies (GISS) climate model. In most gravity wave parameterizations, it is incorrectly assumed that waves propagate only upward, particularly around the polar night jet having strong latitudinal wind shear (Sato et al. 2009). In nonorographic parameterizations, quantitative relations between the physical properties of gravity wave sources and the generated gravity waves (e.g., source spectra, intermittency, and amplitudes) have not been fully clarified (e.g., Scinocca 2003; Beres et al. 2004; Richter et al. 2010). Thus, it is important to further examine sources, generation, propagation, and amplitudes

TABLE 1. Specifications of PANSY.

System	Pulse Doppler radar with active phased-array system
Center frequency	47 MHz
Antenna	An irregular array consisting of 1045 crossed-Yagi antennas.
	Effective diameter about 160 m (18 000 m^2)
Transmitter	1045 solid-state TR modules
	Peak power: 520 kW
Receiver	(55 + 8)-channel digital receiving systems
	Ability of imaging and interferometry observations
Peripheral	24 antennas for E-layer field-aligned irregularities (FAI) observation

of the gravity waves. In this study, using a gravity wave–resolving model, we also examine the generation and propagation mechanisms of gravity waves with sufficiently large amplitude to account for observed multiple tropopause structures in high latitudes.

The present paper is organized as follows. The methods of this study are described in section 2. Observational results are described and a detailed case study is made in section 3. Results of the model simulations are given and compared with the observations, and the spatial structures of a multiple tropopause event are analyzed in section 4. A discussion is in section 5, and section 6 summarizes the results and gives concluding remarks.

2. Methodology

a. The PANSY radar observations

1) A brief description of the PANSY radar system

PANSY is the first MST radar installed in the Antarctic to observe the Antarctic atmosphere in the height range of 1.5–500 km. It is located at Syowa Station. PANSY is a pulse-modulated monostatic Doppler radar with an active phased-array system consisting of 1045 crossed-Yagi antennas distributed in an area equivalent to a circular area of diameter 160 m. PANSY is designed to observe winds with fine time and vertical resolutions of about 1 min and 75 m, respectively. The accuracy of line-of-sight wind velocity is about 0.1 m s^{-1}. The horizontal beamwidth is designed to be about 1°. Because the target of the MST radars is atmospheric turbulence, wind measurements are possible in any weather condition. The specifications of PANSY are given in Table 1. Continuous observations have been made by PANSY since 30 April 2012 in a quarter of its full designed system with a time resolution of 2 min and vertical resolution of 150 m. The horizontal beamwidth has been about 5°. Full system observations will start in 2015 if no severe transport problems occur. It is expected that the dynamics of the Antarctic atmosphere and its various features will be quantitatively examined by observations with this radar in combination with other instruments. See Sato et al. (2014) for details of the PANSY system and expected studies using PANSY.

2) Estimation methods of three-dimensional winds and vertical momentum fluxes

The PANSY data that we used consists of the line-of-sight wind velocities of five beams, which are pointed in a vertical direction and tilted to the east, west, north, and south with the same zenith angle, $\theta = 10°$, and are taken in April and May 2013. In the dual-beam method, horizontal velocities are estimated from line-of-sight velocities of symmetrical beams around the zenith. Line-of-sight velocities $V_{\pm\theta}$ observed by beams with zenith angles of $\pm\theta$ are the horizontal and vertical components of the wind velocity vectors $(u_{\pm\theta}, w_{\pm\theta})$ in the targeted volume range:

$$V_{\pm\theta} = \pm u_{\pm\theta} \sin\theta + w_{\pm\theta} \cos\theta .$$

By assuming that the winds are homogeneous at each height (i.e., $u_{+\theta} = u_{-\theta} \equiv u$ and $w_{+\theta} = w_{-\theta} \equiv w$), we can estimate the horizontal and vertical wind components as

$$u = \frac{V_{+\theta} - V_{-\theta}}{2\sin\theta}, \quad w = \frac{V_{+\theta} + V_{-\theta}}{2\cos\theta} .$$

The vertical flux of horizontal momentum is directly estimated from the variances of the line-of-sight velocities (Vincent and Reid 1983):

$$\overline{V'^2_{\pm\theta}} = \overline{u'^2_{\pm\theta}} \sin^2\theta + \overline{w'^2_{\pm\theta}} \cos^2\theta \pm \overline{u'_{\pm\theta} w'_{\pm\theta}} \sin 2\theta$$

$$\overline{u'w'} = \frac{\overline{V'^2_{+\theta}} - \overline{V'^2_{-\theta}}}{2\sin 2\theta} .$$

Here, we assume that the flux and variance fields are homogeneous. This assumption is less strict than that used for the u and w estimates. Thus, the method using MST radars provides very accurate estimates of momentum fluxes.

3) Other data used in this study

Operational radiosonde observation data at Syowa Station every 0000 and 1200 UTC are also used for the analyses. The vertical sampling interval is about 250 m. The data include temperature and horizontal wind vectors in the height region from the ground up to about 30 km. The tropopause heights are determined according to the WMO definition. Note that radiosonde

TABLE 2. Relation between glevels and actual resolutions of NICAM.

Glevel	Grid number	Resolution (km)
5	10 242	223
6	40 962	112
7	163 842	55.8
8	655 362	27.9
9	2 621 442	13.9
10	10 485 762	6.97
11	41 943 042	3.49

observations provide horizontal wind data below 1.5 km, where the PANSY cannot observe.

We also use ERA-Interim data produced by the European Centre for Medium-Range Weather Forecasts (ECMWF) (Dee et al. 2011) for synoptic atmospheric conditions during the observation period. The ERA-Interim data cover the time period from 1 January 1989 onward. The ERA-Interim data used in the present study are at durations of 6 h with 1.5° horizontal resolution and distributed on 15 isentropic surfaces from 265 up to 850 K and on 40 pressure levels from 1000 to 1 hPa.

b. Numerical experiments using NICAM

1) MODEL DESCRIPTION

For the numerical simulations in this study, we used the Nonhydrostatic Icosahedral Atmospheric Model (NICAM), a global cloud-system resolving model (GCRM) (Satoh et al. 2008). This model employs a nonhydrostatic dynamical core as the governing equations and an icosahedral grid over the sphere. The finite-volume method is used for numerical discretization to conserve total mass, momentum, and energy over the domain.

Horizontal resolutions are represented by grid division level n (glevel-n). Glevel-0 means the original icosahedron. By dividing each triangle into four small triangles recursively, we obtain one higher resolution. The total number of grid points is $N_g = 10 \times 4^n + 2$ for glevel-n. The actual resolution corresponds to the square root of the averaged control volume area, $\Delta x \equiv \sqrt{4\pi R_E^2/N_g}$, where R_E is Earth's radius. Examples of respective glevels and corresponding resolutions are shown in Table 2. Previous studies show that NICAM is able to capture hierarchical structures in cloud systems even with grid intervals of 14 km, which corresponds to glevel-8 (e.g., Tomita et al. 2005). The grids of NICAM can be transformed to finer grids around a target region, with the stretching factor β representing the ratio between maximum and minimum grid intervals. Moreover, unlike regional models, the stretched-grid model does not have the problem of artificial wave reflection at the domain boundaries.

So far, many studies have focused on atmospheric phenomena in the tropics with NICAM. For example, Miura et al. (2007) simulated the Madden Julian oscillation (MJO) by using NICAM with glevel-11 and glevel-10 on the Earth Simulator. In this study, we use the stretched-grid NICAM to see the three-dimensional structure of atmospheric fields with fine vertical resolution, which is comparable to the PANSY observation.

2) MODEL SETTINGS

We use a model of glevel-7 with $\beta = 100$ grid centered at 65°S, 40°E, which is slightly to the north of Syowa Station (69.1°S, 39.6°E), as shown in Fig. 1a. Grid intervals are about 5.6 km at the center of the grids and 6.25 km at Syowa Station (Fig. 1b). The time step is 6 s. As the boundary layer scheme, Mellor–Yamada–Nakanishi–Niino

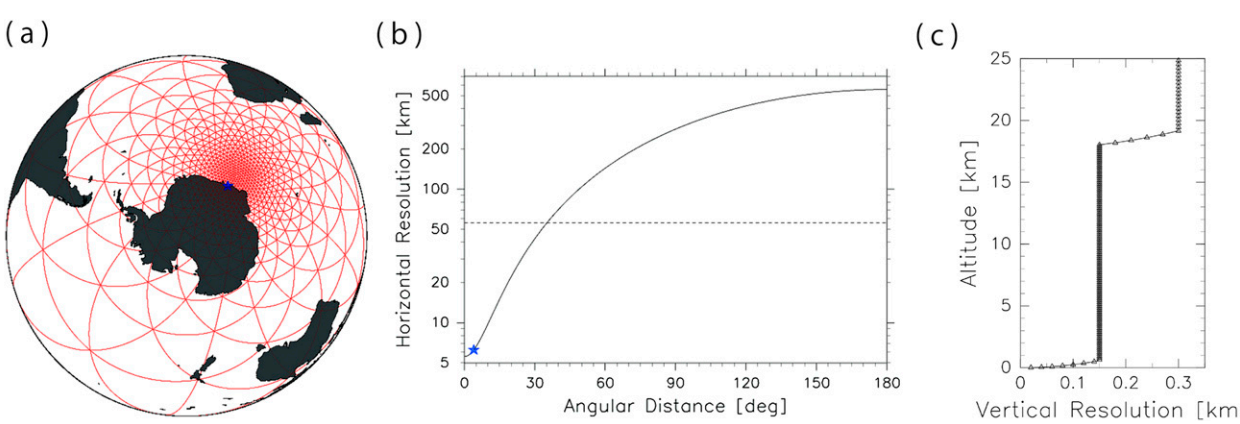

FIG. 1. (a) An illustration of the stretched grid (roughened up to glevel-3). (b) The resolution distribution of the stretched grid (solid) and the quasi-uniform grid with the same glevel (dotted). A star at the bottom corresponds to the location of Syowa Station. (c) Vertical grid spacing of NICAM as a function of the altitude. Each mark denotes the grid point.

(MYNN) level 2 (Nakanishi and Niino 2004) is used. The model top is about 53 km. Rayleigh damping with an *e*-folding time of 1 day for vertical wind components above 50 km is included to avoid the reflections of waves at the top boundary. No cumulus and gravity wave parameterizations are used.

3) VERTICAL COORDINATES

The basic terrain-following (BTF) coordinate (Gal-Chen and Somerville 1975) is used as the vertical coordinate system for the original NICAM (Satoh et al. 2008). The BTF coordinate, however, occasionally causes severe numerical errors over steep mountains (Schär et al. 2002; Klemp 2011). Since the Antarctic topographies are quite steep around the coast, this computational problem may be critical for simulations near the Antarctic coast region. To avoid this problem, the smoothed terrain-following (STF) coordinate proposed by Klemp (2011) is implemented in NICAM. The STF coordinate can significantly reduce the influence of steep terrain with four smoothing parameters (Klemp 2011). We used the following numbers for the smoothing parameters:

$$\left(M_k, \beta_k, \gamma_{\min}, \frac{z_H}{h_m}\right) = (100, 0.2, 0.4, 1.25). \quad (1)$$

To resolve the fine structure of disturbances above the tropopause, the vertical grid spacing is 150 m at heights from 560 m to about 20 km and 300 m at heights from about 20 km to the model top (Fig. 1c). Unphysical reflection of waves due to the change of the vertical grid spacing hardly occurs in this simulation (not shown). The number of vertical levels is 243. As shown later, this model has high horizontal and vertical resolutions that are sufficient to resolve gravity waves having short wavelengths, as observed by PANSY and radiosondes at Syowa Station.

4) INITIAL CONDITION AND TIME INTEGRATION

The NCEP Final (FNL) Operational Global Analysis is used in the present study as the initial values for the NICAM simulations. This is produced in the Global Data Assimilation System (GDAS) every 6 h. The datasets are distributed on $1° \times 1°$ horizontal grids at the surface and on 26 vertical levels up to 10 hPa. Simulations were performed for the time period from 0000 UTC 7 April to 0000 UTC 12 April. The model output was stored every 1 h. We confirmed that there are no discernible difference between the ERA-Interim and NCEP GDAS. The use of NCEP GDAS is simply because the computational code in NICAM (Tomita et al. 2005) uses NCEP GDAS as an initial condition.

3. Observational results

a. Overview in April and May 2013

Figure 2 shows the time–height cross sections of the zonal and meridional wind components estimated by the dual-beam method using PANSY observations in the time period from 31 March to 16 May 2013 in the height region from about 1.5 to about 15 km. The red circles denote the thermal tropopauses, estimated by the operational radiosonde observations. Multiple thermal tropopause structures are observed in association with the descent of the first (lowest) tropopause five times during this period: namely, on 1 April, 9–11 April, 24–27 April, 5–6 May, and 10–13 May. The altitudes of observed multiple tropopauses are much higher than those of the first tropopauses over Syowa Station ($z < 10$ km). Simultaneously, the eastward wind is enhanced, and the meridional wind underwent large fluctuations around 10 km in all five events (Fig. 2).

Rao et al. (2008) pointed out that such a descent along with an increase in zonal wind observed by radars and/or radiosondes indicates a tropopause folding. To confirm this for the present cases, the structure of potential vorticity (PV) is examined for multiple tropopause events by using ERA-interim data. Figure 3a shows snapshots of the horizontal map of PV at 1200 UTC 9 April, 0600 UTC 25 April, and 1200 UTC 6 May on an isentropic surface of $\theta = 315$ K. A strong PV gradient and the meandering polar front jet around the 2 PV unit (PVU; 1 PVU = 10^{-6} K kg^{-1} m^2 s^{-1}) isolines are observed near Syowa Station for all events. Figure 3b shows longitude–height sections (9 and 25 April) and a latitude–height section (6 May) of the PV across Syowa Station. These cross sections are chosen because they are nearly orthogonal to the PV isolines shown in Fig. 3a. Although the horizontal resolution of the ERA-Interim dataset ($1.5° \times 1.5°$) may be too coarse to resolve the tropopause folding structure clearly, the drastic jumps of 2-PVU isolines observed in Fig. 3b suggest that the tropopause folding occurs at each event. It should be noted that there are a couple of time periods (5–7 April and 29–30 April) when eastward wind enhancements are observed but multiple tropopauses and descents of the first tropopause are not accompanied. During these periods, the polar night jet does not strongly meander, and the drastic jump of PV, as observed for the multiple tropopause events in Fig. 3, is not observed (not shown).

Thus, these multiple tropopause events are likely related to the tropopause folding and synoptic scales of PV disturbances. In the following, we focus on a typical event observed in April.

b. Case study on 7–11 April 2013

Figure 4 shows the time–height cross sections of the zonal and meridional wind components estimated from

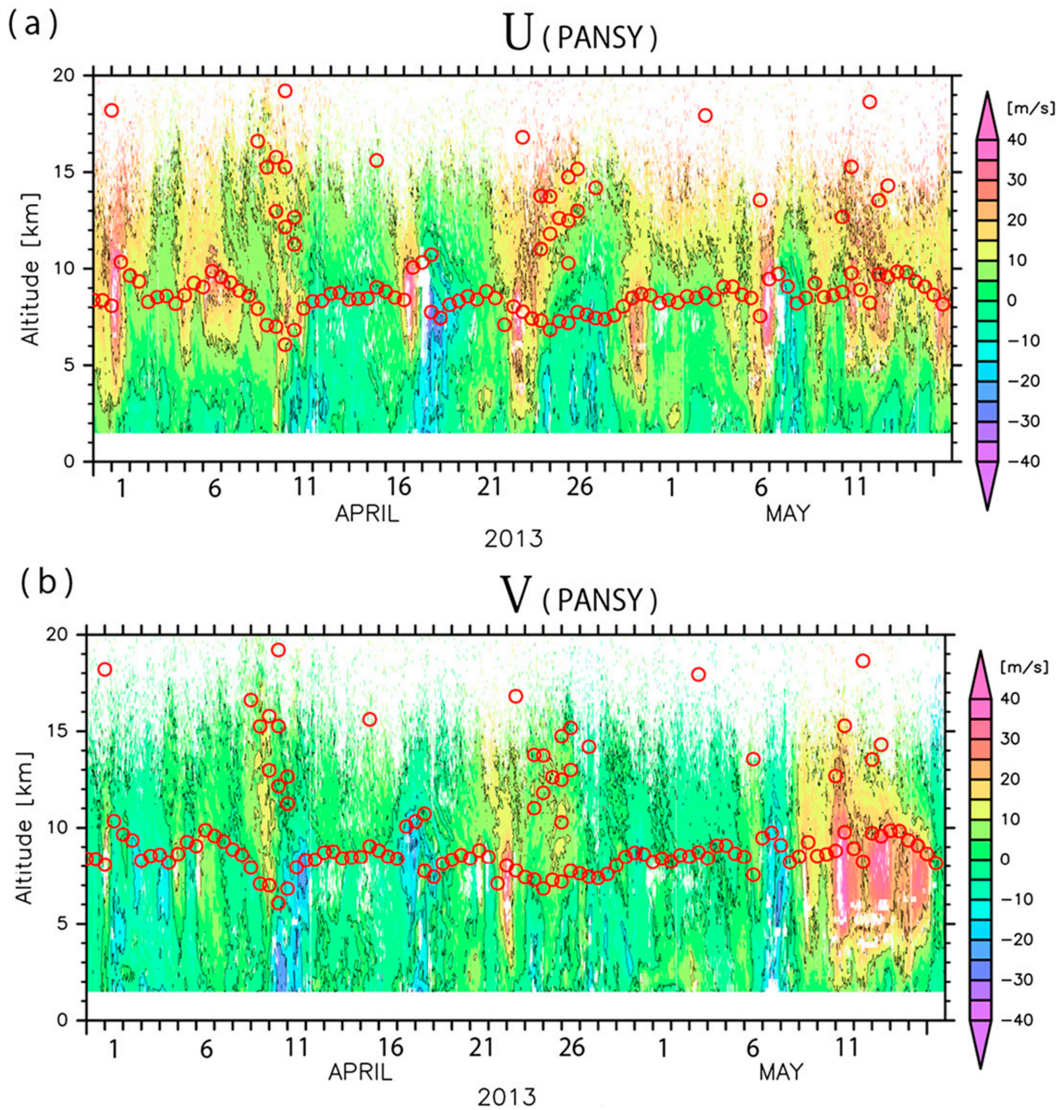

FIG. 2. Time–altitude cross sections of (a) zonal U and (b) meridional wind V components observed by PANSY at Syowa Station (contour interval $10\,\mathrm{m\,s^{-1}}$). The red circles denote the tropopause as determined by twice-daily operational radiosonde observations.

the PANSY observations and the static stability from the radiosonde observations for 0000 UTC 7 April–2400 UTC 11 April. In Figs. 4a and 4b, clear wavelike wind disturbances having phases propagating downward are observed, and the multiple tropopause structure appears in the height region of 10–15 km. The vertical wavelengths and wave periods of these disturbances are about 3 km and about 10 h, respectively. In Fig. 4c, the descent of the first tropopause corresponds to the descent of the maximum of the static stability, which is more than $6.0 \times 10^{-4}\,\mathrm{s^{-2}}$.

As shown in previous studies for midlatitudes (e.g., Sato and Yamada 1994; Vaughan and Worthington 2007; Pavelin et al. 2001), such wind fluctuations in the lower stratosphere are mainly due to inertia–gravity waves. Thus, under the working hypothesis that these wind fluctuations are due to inertia–gravity waves, we estimate the wave parameters by hodograph analyses. This hypothesis can be validated by comparing estimated wave parameters from three independent methods and by comparing directly observed and indirectly estimated ground-based wave periods.

According to the linear theory of the inertia–gravity wave, a hodograph has the shape of an ellipse. The lengths of the major and minor axes of the ellipse correspond to the amplitudes of the horizontal wind components, which are parallel to ($u_\parallel$) and orthogonal to ($u_\perp$) the horizontal wavenumber vector, respectively. Based

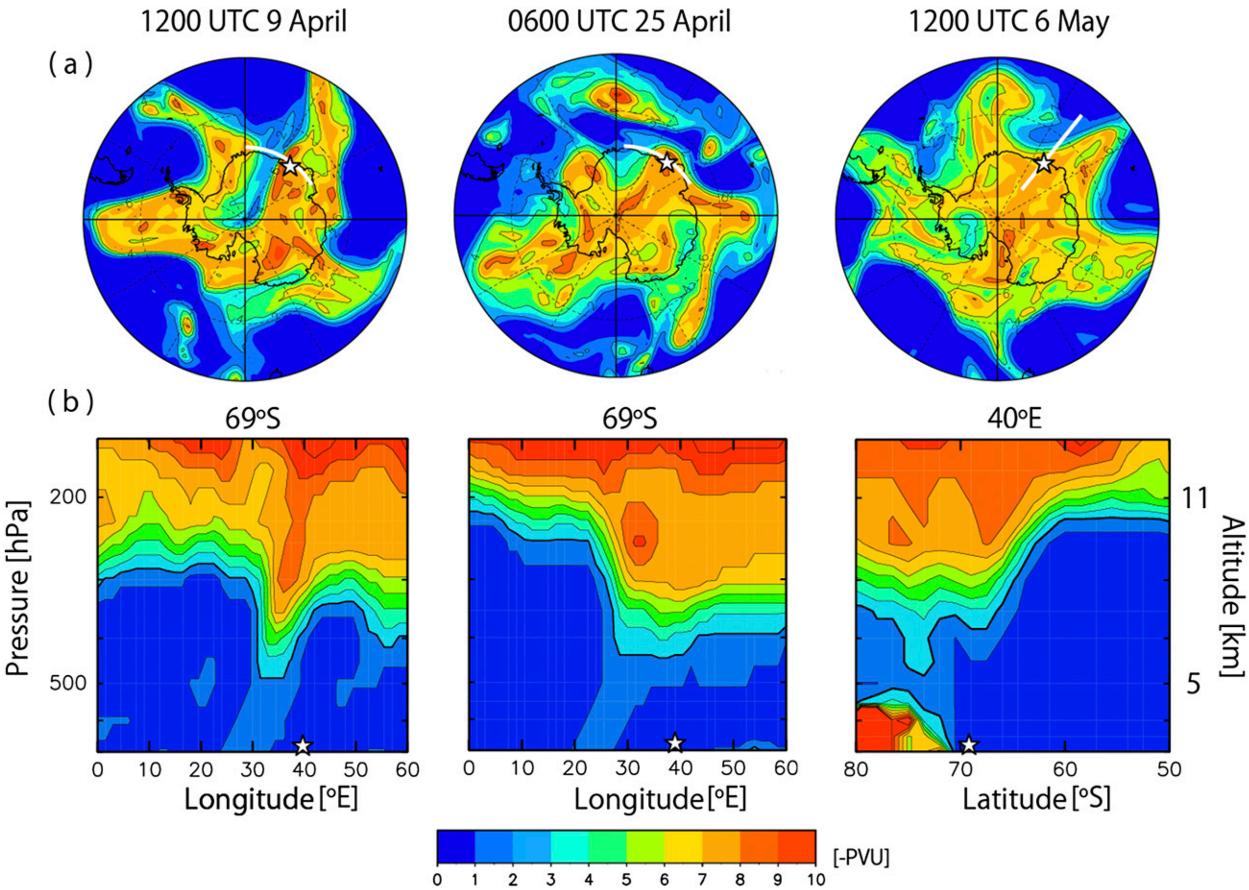

FIG. 3. Snapshots of (a) horizontal map at an isentropic surface of 315 K; and (b) (left),(middle) longitude–height and (right) latitude–height cross sections of potential vorticity (contour intervals 1 PVU) at 1200 UTC 9 Apr, 0600 UTC 25 Apr, and 1200 UTC 6 May 2013 using ERA-Interim data, respectively. A star in each of the panels denotes the location of Syowa Station (69°S, 39.6°E). White lines in (a) denote the longitude or latitude for which the cross section is shown in (b). Thick black curves in (b) denote isolines of 2 PVU.

on the polarization relation, the intrinsic frequency $\hat{\omega}$ can be determined from the ratio of the length of the major axis to the minor axis:

$$\hat{\omega} = \left| \frac{u_{\parallel}}{u_{\perp}} f \right|, \tag{2}$$

where f denotes the inertial frequency. The intrinsic frequency is taken to be positive without losing generality (e.g., Sato et al. 1997). The direction of vertical energy propagation can be estimated from the rotation of the hodograph in the vertical: in the Southern Hemisphere, an anticlockwise (clockwise) rotation with increasing height means upward (downward) energy propagation.

The other wave parameters such as the horizontal wavenumber k can be indirectly estimated by using the dispersion relation of inertia–gravity waves, although an ambiguity for 180° remains in the direction. For hydrostatic inertia–gravity waves, the dispersion relation in a uniform background is written as follows:

$$\hat{\omega}^2 = f^2 + \frac{N^2 k^2}{m^2}, \tag{3}$$

where N is the Brunt–Väisälä frequency, and k and m are the horizontal and vertical components for the wavenumber vector, respectively. The value of N^2 is estimated to be about $3.5 \times 10^{-4}\,\mathrm{s}^{-2}$ from the radiosonde observations, and the inertial frequency is $1.358 \times 10^{-4}\,\mathrm{s}^{-1}$ at Syowa Station.

The horizontal wavenumber k can also be estimated by another method. According to the polarization relation, a Lissajous curve of $u_{\parallel}$ and temperature fluctuations (T') should also have the shape of an ellipse:

$$-i\hat{\omega}\frac{T'}{\overline{T}}g - N^2\frac{k}{m}u_{\parallel} = 0, \tag{4}$$

where g is the gravitational acceleration and $\overline{T}$ is the background temperature. This means that $u_{\parallel}$ and T' are

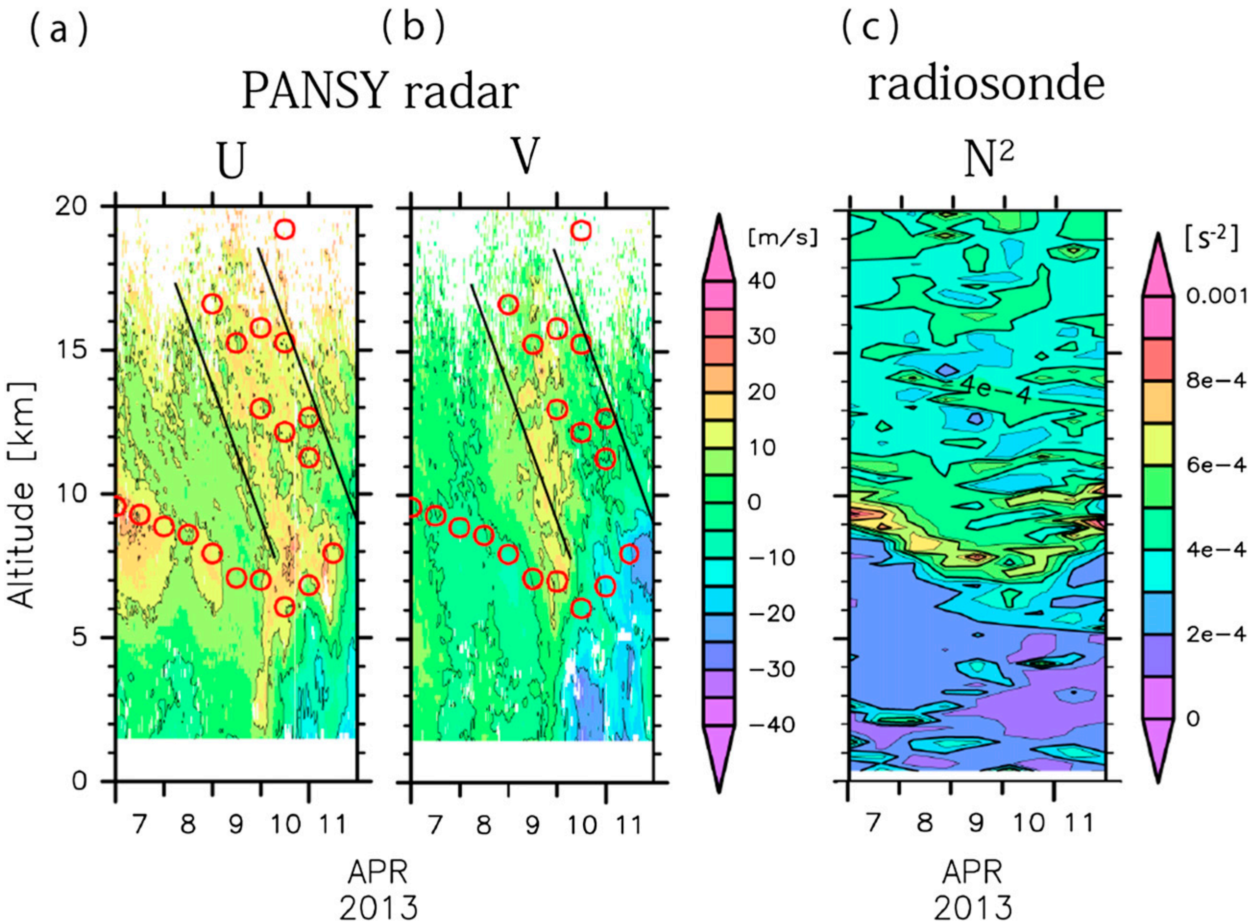

FIG. 4. Time–altitude cross sections of (a) zonal wind velocity and (b) meridional wind velocity (contour interval $10\,\mathrm{m\,s^{-1}}$) from the PANSY observations and (c) Brunt–Väisälä frequency from twice-daily operational radiosonde observations (contour interval $1.0 \times 10^{-4}\,\mathrm{s^{-2}}$). Black lines in (a),(b) highlight phase lines of wave structures.

out of phase by 90°. The horizontal wavenumber k can be obtained as follows:

$$k = \frac{m\hat{\omega}g}{N^2}\frac{|T'/\overline{T}|}{|u_\parallel|}, \tag{5}$$

where vertical bars around the variables denotes the amplitude of the fluctuation. It is worth noting that this estimation for the horizontal wavenumber k is made using different quantities ($u_\parallel$ and T') from those based on the dispersion relation (3) (i.e., $u_\parallel$ and $u_\perp$).

The ground-based frequency ω is directly obtained in the time–height section of observed wind fluctuation components. The ground-based frequency ω is estimated by using the Doppler relation:

$$\omega = \hat{\omega} + Uk, \tag{6}$$

where U denotes the background horizontal wind parallel to the horizontal wavenumber vector. It should be noted that the estimation of the ground-based frequency by (6) is also independent of the direct estimation from the time–height section.

Figure 5a shows the hodograph from the radiosonde observation data extracted by a bandpass filter with cutoff wavelengths of 1.5 and 5 km in the vertical at 0000 UTC 10 April. The hodograph shows an anticlockwise rotation with height, which means upward energy propagation. The shape of the ellipse is determined by the least squares method using an elliptical fitting. The wave parameters are estimated by (2), (3), and (6). The vertical wavelength is about 2.5 km. The estimated $\hat{\omega}$ is $3.6 \times 10^{-4} \pm 0.2 \times 10^{-4}\,\mathrm{s^{-1}}$. The estimated horizontal wavenumber k by using the dispersion relation is $4.1 \times 10^{-5} \pm 0.4 \times 10^{-5}\,\mathrm{m^{-1}}$. The estimated horizontal phase speed is $5.3 \pm 0.9\,\mathrm{m\,s^{-1}}$. The ambiguity of the respective estimations corresponds to the residual of the elliptic fitting from the observation data.

Figure 5b shows the Lissajous curve of the horizontal wind fluctuation component $\tilde{u}$ parallel to the horizontal wavenumber vector determined by the hodograph

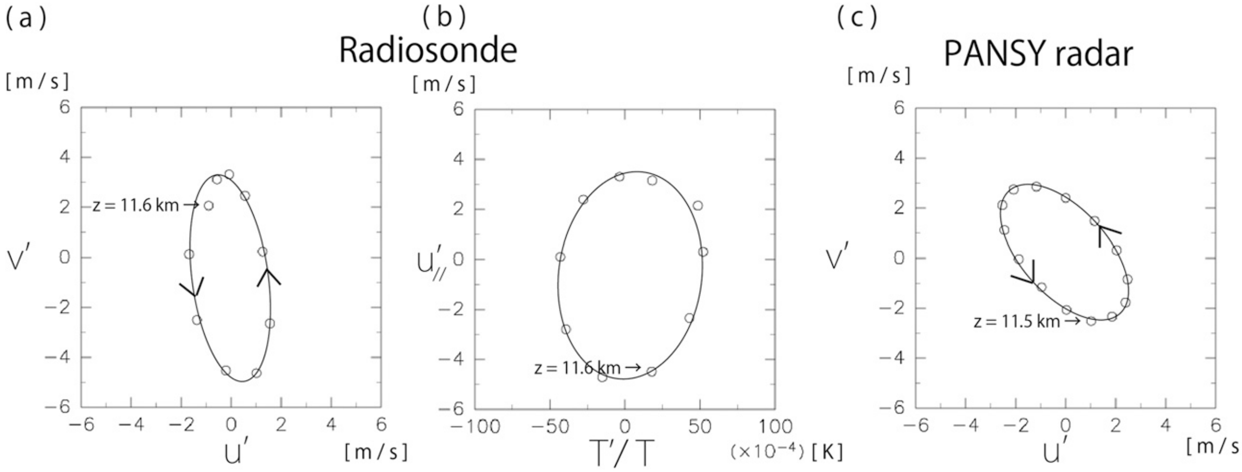

FIG. 5. (a) A hodograph of the horizontal wind fluctuations. (b) A Lissajous curve of temperature and horizontal wind fluctuations parallel to the wavenumber vector in the height region of 11.6–14.1 km at 0000 UTC 10 Apr from the radiosonde observation. (c) The horizontal wind fluctuations in 11.5–13.8 km at 2000 UTC 9 Apr 2013 from the PANSY observation. Each mark is plotted with about a 250-m interval for (a) and (b) and a 150-m interval for (c). Arrows in (a) and (c) show the direction of a rotation on the hodograph.

shown in Fig. 5a and the normalized temperature fluctuation, $T'/\overline{T}$. It is seen that $\tilde{u}$ and T' are roughly out of phase by a quarter wavelength, which is consistent with the polarization relation of the inertia–gravity wave. The horizontal wavenumber k estimated by (5) is $3.1 \times 10^{-5} \pm 0.4 \times 10^{-5}\,\mathrm{m}^{-1}$. The estimated horizontal phase speed is $8.5 \pm 1.4\,\mathrm{m\,s}^{-1}$. These results roughly agree with those of the hodograph analysis.

We also conducted an analysis using the PANSY data. Figure 5c shows the horizontal wind fluctuations extracted by using a bandpass filter with cutoff wavelengths of 1.5 and 5.0 km and by a high-pass filter with a cutoff wave period of 25 h. A hodograph at 2000 UTC 9 April is shown in Fig. 5c. An anticlockwise rotation is clearly observed and indicates that the inertia–gravity wave propagates energy upward. The vertical wavelength is about 2.1 km. The estimated $\hat{\omega}$ and k are $2.6 \times 10^{-4} \pm 0.2 \times 10^{-4}\,\mathrm{s}^{-1}$ and $3.5 \times 10^{-5} \pm 0.3 \times 10^{-5}\,\mathrm{m}^{-1}$, respectively. The estimated horizontal phase speed is $6.3 \pm 1.0\,\mathrm{m\,s}^{-1}$. These values are roughly consistent with the abovementioned results of the analysis using the radiosonde data.

The orientation of the major axis indicates that the wavenumber vector is northwestward or southeastward with an ambiguity of 180°. Thus, the ground-based frequency is calculated for both cases. If southeastward wave propagation is assumed, the ground-based period is 7.8 ± 0.5 h. If northwestward wave propagation is assumed, the ground-based period is 5.8 ± 0.5 h. The ground-based period of fluctuations estimated directly from PANSY observations is about 7.7 h. This means that the wave packet likely propagates southeastward.

Table 3 summarizes the wave parameters estimated independently from the PANSY radar and radiosonde data. The ground-based periods from the radiosonde data are obtained by (6). It is clear that the horizontal wavelengths, ground-based wave period, and horizontal phase speed agree rather well for all independent estimation methods. This agreement also indicates the validity of the working hypothesis that the wave disturbances are due to inertia–gravity waves.

Last, the quantitative consistency between the temperature fluctuations forming the thermal tropopauses

TABLE 3. The wave parameters of the inertia–gravity wave estimated from PANSY and the radiosonde through the dispersion relation and the thermodynamic equation.

	PANSY	Dispersion relation	Thermodynamic equation
Vertical wavelength	2.1 km	2.5 km	
Horizontal wavelength	177 ± 18 km	155 ± 15 km	205 ± 25 km
Ground-based wave period	7.7 h (observed), 7.8 ± 0.5 h (estimated)	8.4 ± 0.6 h	6.7 ± 0.3 h
Vertical propagation	Upward	Upward	
Horizontal propagation	Southeastward	Southeastward	
Horizontal phase speed	$6.3 \pm 1.0\,\mathrm{m\,s}^{-1}$	$5.3 \pm 0.9\,\mathrm{m\,s}^{-1}$	$8.5 \pm 1.4\,\mathrm{m\,s}^{-1}$

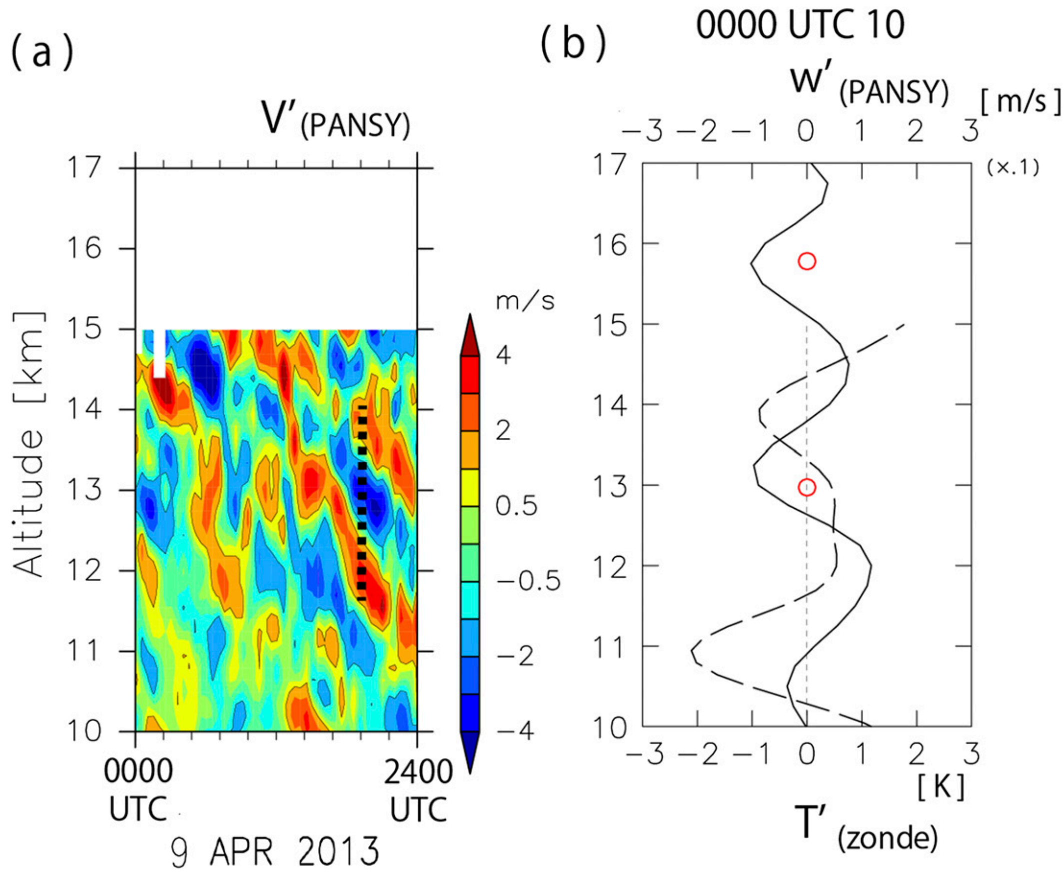

FIG. 6. (a) Time–altitude cross sections of meridional wind fluctuations V' observed by PANSY (contour interval $1\,\mathrm{m\,s^{-1}}$). (b) Observed vertical profiles of temperature fluctuations T' (black line) and vertical wind fluctuations w' (dashed line) at 0000 UTC 10 Apr 2013. The fluctuations are extracted using a bandpass filter with (a) cutoff wavelengths of 1.5 and 5 km and with a cutoff period of 25 h and (b) cutoff wavelengths of 1.5 and 5 km, respectively. The broken line in (a) denotes a profile in which a hodograph analysis is made in Fig. 5c. The red circles denote the tropopause.

and the wind fluctuations associated with the inertia–gravity waves are examined. Vertical profiles of the temperature fluctuations T' from the radiosonde observation and the vertical wind fluctuations w' from the PANSY observations are shown in Fig. 6b. It seems that T' is out of phase with w' by 90° around the thermal tropopauses, and the height of the minimum T' is lower than that of w'. These features are consistent with the thermodynamic equation [(7)] with negative vertical wavenumber m, which is consistent with the rotation of the hodograph (Fig. 5). The amplitude of T' is estimated as follows:

$$-i\hat{\omega}\frac{T'}{\overline{T}}g + N^2 w' = 0$$

$$|T'| = \frac{N^2\overline{T}}{g\hat{\omega}}|w'|, \qquad (7)$$

By using an observed amplitude of w' of about $0.075\,\mathrm{m\,s^{-1}}$ and by considering the errors of the estimated intrinsic frequencies, the amplitude of T' is estimated as $1.55 \pm 0.15\,\mathrm{K}$. This estimation agrees well with the observation shown in Fig. 6b. This result also supports the presumption that the multiple tropopauses observed in Fig. 6 are due to inertia–gravity waves.

4. Results of numerical experiments

a. *Tropopause folding and descent of a first tropopause height*

To examine the spatial structures and generation mechanisms of the inertia–gravity waves forming the multiple tropopauses observed at Syowa Station, a model simulation was performed. Figures 7a and 7b respectively show the longitude–height cross sections of the PV at 69°S and the horizontal maps of the PV at 315 K at 1200 UTC 7 April, 2400 UTC 7 April, 1200 UTC 8 April, and 1200 UTC 9 April. Note that the horizontal model resolution in the region far from Syowa Station is coarse in the stretched grid. According

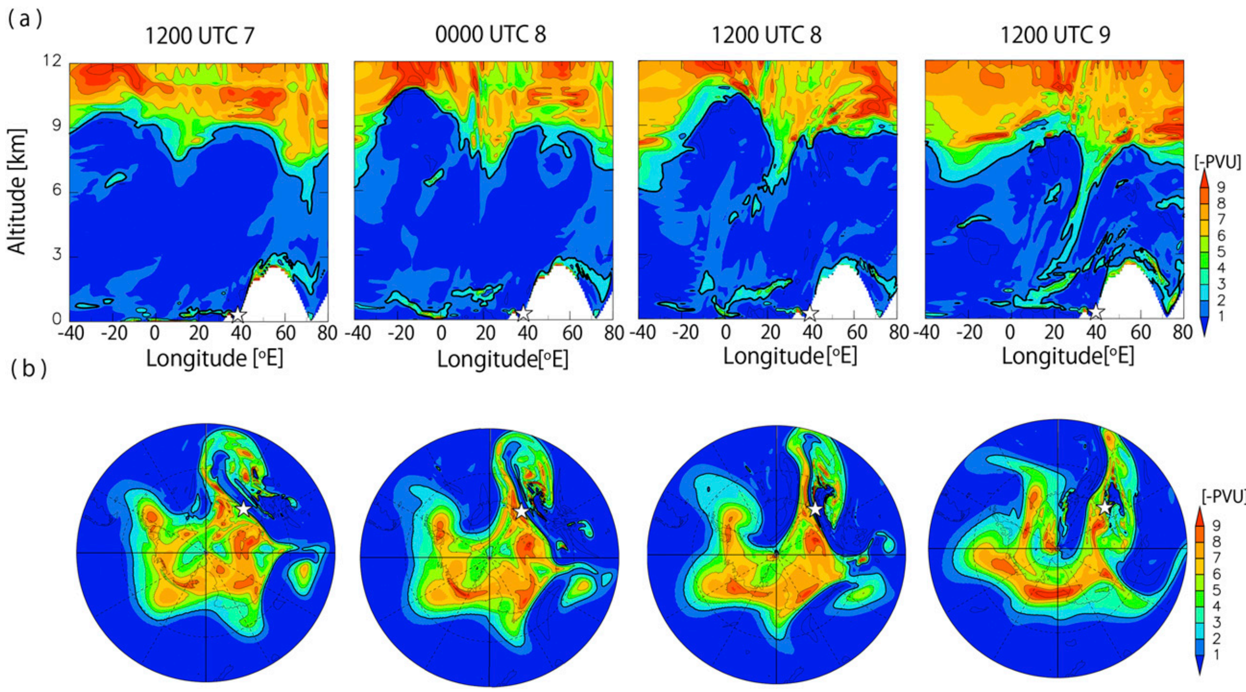

FIG. 7. Snapshots of (a) longitude–height cross sections at 69°S and (b) horizontal maps at $z = 8.4$ km of potential vorticity field at (left to right) 1200 UTC 7 Apr, 0000 UTC 8 Apr, 1200 UTC 8 Apr, and 1200 UTC 9 Apr 2013. Contour intervals are 2 and 1 PVU for (a) and (b), respectively. A star denotes the location of Syowa Station (69°S, 39.6°E).

to Wilcox et al. (2012), the tropopause in the polar region roughly corresponds to 2-PVU isolines. It is seen in Fig. 7b that an anticyclonic PV anomaly (a dark blue region) is located around 60°W at 1200 UTC 7 April, moves eastward and southward from 0000 to 1200 UTC 8 April, and breaks around 30°E at 1200 UTC 9 April. A developing ''folding'' structure is observed in Fig. 7a at 1200 UTC 9 April when the PV gradient gets stronger in association with the anticyclonic breaking. This sharp PV gradient corresponds to the axis of the strong polar front jet, which meanders significantly.

In Fig. 7a, it is clear that the height of the dynamical tropopause (2-PVU contours) over Syowa Station descends from 1200 UTC 7 April to 1200 UTC 9 April as the system in which the tropopause folding evolves moves eastward. Thus, it is considered that the descent of the first tropopause observed at Syowa station is attributable to such a time evolution and passage of the tropopause folding.

b. Model simulation: Comparison to the observation

Figures 8a–c show the time–height cross sections of the zonal and meridional wind components and the Brunt–Väisälä frequency. A comparison of the observations (Fig. 4) shows that the model successfully simulated these basic physical quantities, including the features of the descent of the first tropopause and the wavelike structures with phases propagating downward in the lower stratosphere. The multiple tropopause structures are also well simulated with respect to timing and altitudes. It should be noted that, since the model top is located at $z \approx 53$ km, artificial trapped waves hardly appear in the region below $z = 25$ km that is depicted in Fig. 8.

Figure 8d shows the temperature fluctuations extracted by a bandpass filter with cutoff wavelengths of 1.5 and 5 km in the vertical and a high-pass filter with a cutoff period of 25 h in time. The heights of the multiple tropopauses correspond to the local minima of the temperature fluctuations and are consistent with the observations shown in section 3b.

To examine the horizontal structures of these wavelike disturbances, snapshots of dw/dz, which corresponds to the opposite of horizontal wind divergence, and isobars are shown in Fig. 9 at the altitudes of $z =$ 13.5, 17.5, and 21.5 km at 1200 UTC 9 April, where thermal tropopauses were detected at this time (Figs. 8a,b). The positive and negative dw/dz values are shown by warm and cold colors, respectively. Note that gravity waves are characterized as atmospheric waves having significant horizontal wind divergences.

It is clear that wavelike structures are observed not only over Syowa Station but also over the ocean around 60°S at all the height levels shown in Fig. 9. Thus, from the phase structures in Figs. 8d and 9, the horizontal wavelength and the wave period of the inertia–gravity

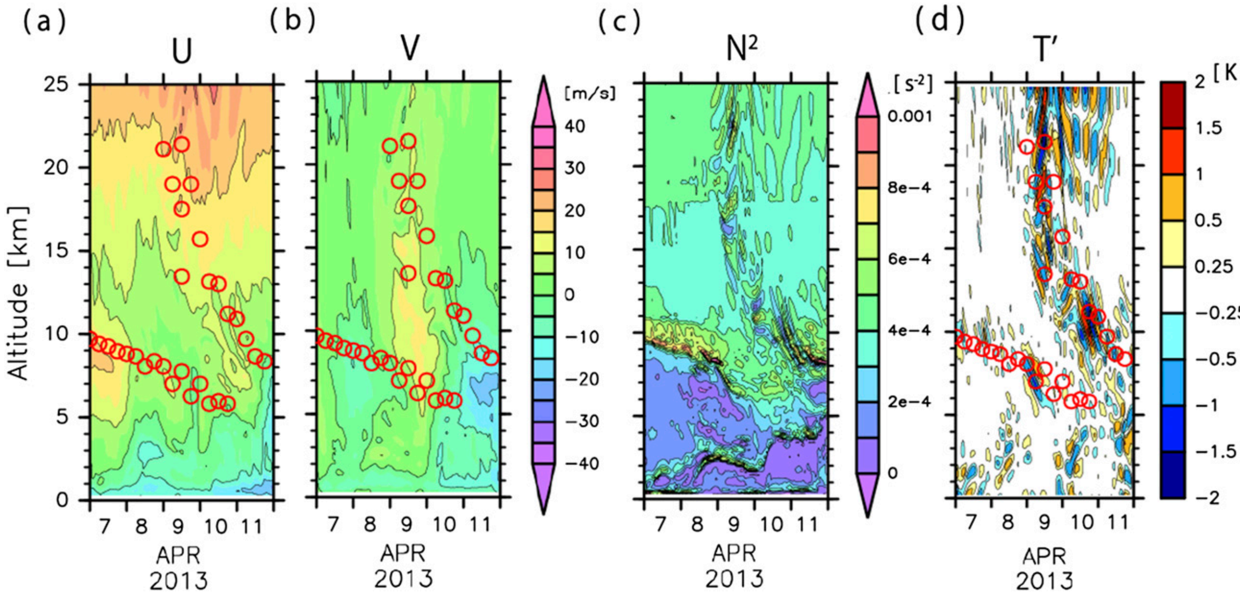

FIG. 8. Time–altitude cross sections of (a) zonal wind velocity U, (b) meridional wind velocity V (contour interval $10\,\mathrm{m\,s^{-1}}$), (c) Brunt–Väisälä frequency (contour interval $1.0 \times 10^{-4}\,\mathrm{s^{-2}}$), and (d) temperature fluctuations extracted by a bandpass filter with cutoff lengths of 1.5 and 5 km and by a high-pass filter with a cutoff period of 25 h. The red circles denote the tropopause at an interval of 12 h.

waves over Syowa Station are estimated as about 200 km and 9 h, respectively. The phase lines over Syowa Station are aligned from southwestward to northeastward and suggest that the direction of the wavenumber vectors is southeastward or northwestward.

Next, we examine the validity of the hodograph analyses using only vertical profiles from the simulations, not the full information available from the four-dimensional output. Hodograph analyses have been carried out in many other observational studies, but the assumption of monochromaticity has sometimes been debated (e.g., Eckermann and Hocking 1989).

Figure 10 shows a hodograph of the simulated horizontal wind fluctuation components at 1500 UTC 9 April at $z = 13.0$–15.2 km. Here, the horizontal wind fluctuation components are extracted with the same filters used for the analysis of the observation data in section 3b. The anticlockwise rotation that is clearly seen in Fig. 10 indicates that the inertia–gravity wave propagates upward energy. The vertical wavelength is about 2.3 km. The estimated $\hat{\omega}$ and k are $2.2 \times 10^{-4} \pm 0.2 \times 10^{-4}\,\mathrm{s^{-1}}$ and $2.6 \times 10^{-5} \pm 0.4 \times 10^{-5}\,\mathrm{m^{-1}}$, respectively. The estimated horizontal phase speed is $6.6 \pm 1.2\,\mathrm{m\,s^{-1}}$. The direction of the wavenumber vector is also estimated by

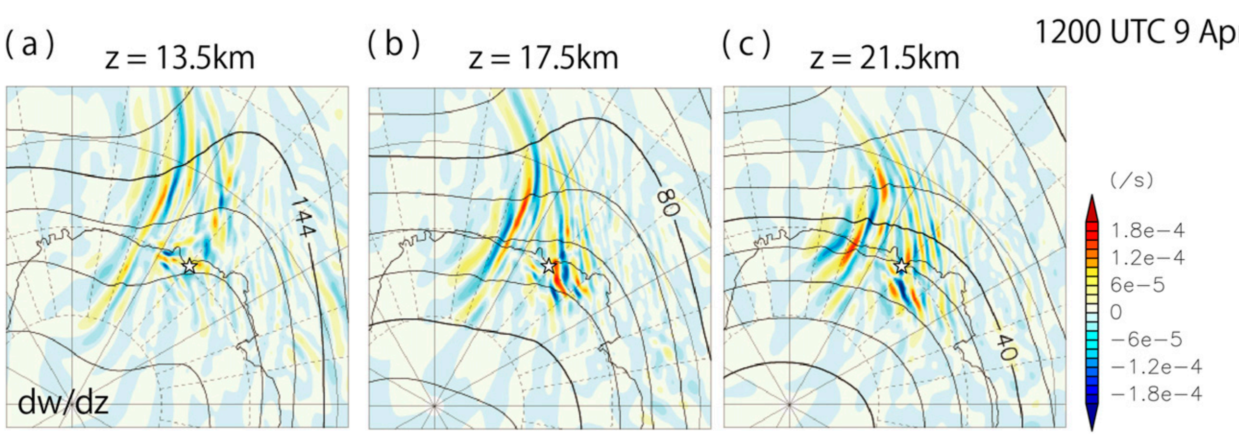

FIG. 9. Snapshots of vertical gradient of vertical wind components dw/dz (color shading) and pressure (contours) at $z =$ (a) 13.5, (b) 17.5, and (c) 21.5 km at 1200 UTC 9 Apr 2013. A star denotes the location of Syowa Station (69°S, 39.6°E). Contour intervals are (a) 4, (b) 2, and (c) 1 hPa.

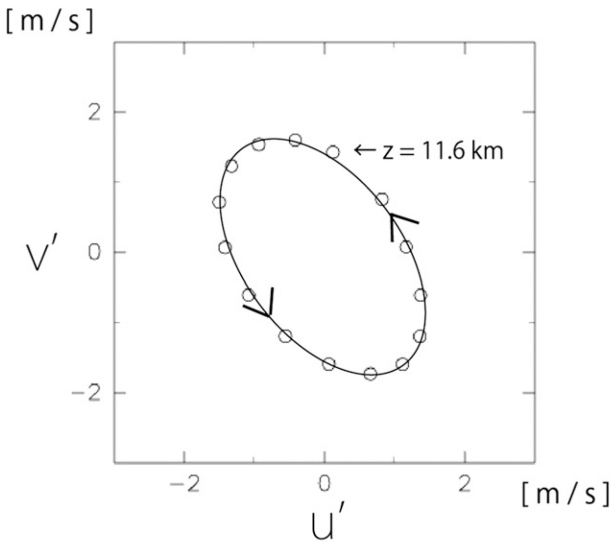

FIG. 10. A hodograph of the horizontal wind fluctuations in the height region of 13.0–15.2 km at 1600 UTC 9 Apr 2013 simulated by NICAM. Each mark is plotted at an interval of 150 m. Arrows show the direction of a rotation on the hodograph.

the same method used in section 3b. The estimated direction is southeastward. The estimated ground-based wave period is 10.1 ± 0.5 h. The estimated parameters using the hodograph analysis in NICAM agree well with those in the horizontal maps of the NICAM simulations. This fact indicates that the assumption of monochromaticity is valid in this case. As shown later (Fig. 9), this is consistent with the fact that most wave structures in this simulation seem to be monochromatic. Thus, this result suggests that the hodograph analysis can provide accurate gravity wave parameters.

Table 4 summarizes the wave parameters that are directly observed and estimated in NICAM. All wave parameters obtained from the model simulation agree quite well with those estimated by the PANSY and radiosonde observations (Table 3). Thus, the results in cross sections 4a and 4b indicate that NICAM successfully simulated not only the synoptic-scale fields, but also the inertia–gravity waves.

c. *Gravity wave propagation*

To examine the origin of the inertia–gravity waves observed at Syowa Station, we made horizontal maps of dw/dz and isobars at $z = 17.5$ km, at 1200 UTC 8 April, 2100 UTC 8 April, and 0600 UTC 9 April, shown in Fig. 11a. The horizontal maps of isobars at $z = 5$ km are also shown in Fig. 11b. Near the ground, strong downslope winds toward the ocean are seen around the slope of about 73°S in this period (Fig. 11b, section 4d). At 1200 UTC 8 April, clear wavelike structures appear first over the ocean around 65°S, 15°E and over the coast of the Antarctic continent around 70°S, 15°E. Here, we first focus on the wave packets over the coast of the Antarctic continent. At 2100 UTC 8 April, the wave packet having phases aligned in the northwest–southeast direction propagates northeastward over the ocean. At 0600 UTC 9 April, the wave packet over the coast propagates eastward, roughly parallel to the latitude lines around 70°S, and reach the location near Syowa Station. The corresponding group velocity of the wave packets over the coast is about 12 m s^{-1}.

TABLE 4. The wave parameters of the inertia–gravity wave estimated from the PANSY radar and observed in the simulation.

	Observation in NICAM	Estimation in NICAM
Vertical wavelength	2.5 km	2.25 km
Horizontal wavelength	200 km	240 ± 30 km
Ground-based wave period	9 h	10.1 ± 0.5 h
Vertical propagation	Upward	
Horizontal propagation	Southeastward	
Horizontal phase speed	6.5 m s^{-1}	6.6 ± 1.2 m s^{-1}

Sato et al. (2012) discussed a mechanism of the leeward propagation of stationary gravity waves, such as topographically forced gravity waves (Sato et al. 2012, their Fig. 6): when the horizontal wavenumber vectors are not parallel to the background wind, the wave energy can be significantly advected by the background wind perpendicular to the wavenumber vector (i.e., parallel to the phase lines). The propagation of wave packets observed over the coast of the Antarctic continent around 30°E in Fig. 11 can be understood by this mechanism. In fact, the background horizontal wind component parallel to the phase lines of the wave packet is about 14 m s^{-1}, which roughly agrees with the wave packet propagation velocity (i.e., group velocity).

Thus, it is possible that the wave packets observed around $z = 17.5$ km at Syowa Station include such stationary waves. To confirm this possibility, we examine the direction of wavenumber vectors observed over Syowa Station on 9 April. Because the vertical momentum flux vector $(\overline{u'w'}, \overline{v'w'})$ is parallel to the wavenumber vector according to the linear inertia–gravity wave theory, the angle of the wavenumber vector from the southward direction ϑ ($-180° \le \vartheta \le 180°$) is calculated as

$$\vartheta = \tan^{-1}\left(\frac{\overline{u'w'}}{-\overline{v'w'}}\right) \times \frac{180°}{\pi}. \qquad (8)$$

The fluctuations are extracted using time and spatial filters, which are the same as those used in section 3b. Figure 12 shows the time–height section of angle ϑ on

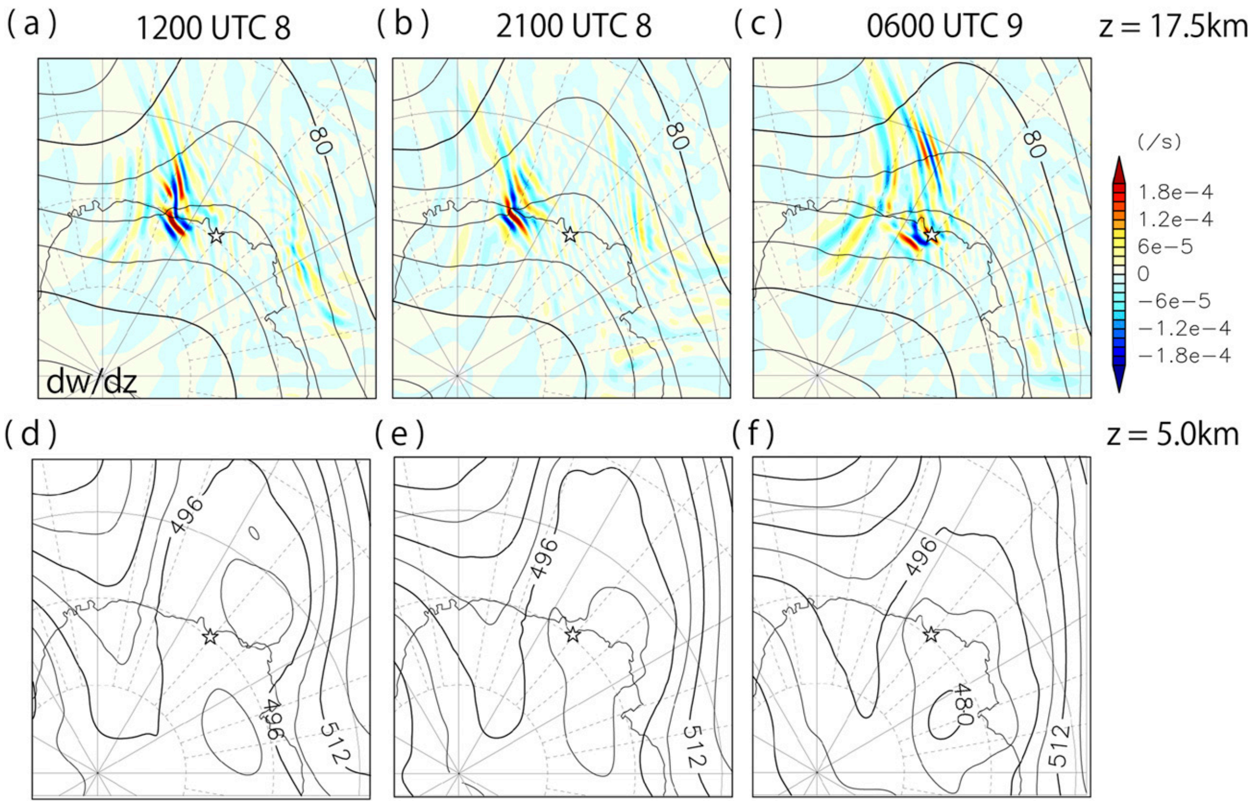

FIG. 11. (top) Snapshots of horizontal maps of vertical gradient of vertical wind components (color shading) and isobars at $z = 17.5$ km at (a) 1200 UTC 8 Apr, (b) 2100 UTC 8 Apr, and (c) 0600 UTC 9 Apr 2013. (bottom) Snapshots of horizontal maps of isobars at $z = 5.0$ km at (d) 1200 UTC 8 Apr, (e) 2100 UTC 8 Apr, and (f) 0600 UTC 9 Apr 2013. A star denotes the location of Syowa Station (69°S, 39.6°E). Contour intervals are 2 hPa in (a),(b),(c) and 8 hPa in (d),(e),(f).

9 April. It is seen that the wavenumber vectors are almost southward ($\vartheta \leq 10°$) in the height region of 16–18 km around 1200 UTC 9 April. This result supports our speculation that the stationary wave packets generated around 70°S, 15°E reached over Syowa Station.

Figure 13a shows the longitude–height cross sections of dw/dz at 65°S. The black contours around $z = 10$ km show 2-PVU isolines corresponding to the dynamical tropopause. At 1200 UTC 8 April, some gravity waves in the lower stratosphere are observed around 20°E, whereas other gravity waves are located around the dynamical tropopause. At 2100 UTC 8 April and at 0600 UTC 9 April, it is seen that the gravity waves in the height region of 15–25 km around 30°E propagate upward and eastward, whereas some of the gravity waves are still located near the dynamical tropopause around $z = 10$ km and move eastward together with the tropopause folding system.

Plougonven and Snyder (2005) suggested that in regions where the horizontal deformation field is large, such as in the baroclinic wave system, the structure of inertia–gravity waves is strongly influenced by the background flow. According to Bühler and McIntyre (2005), the evolution of $\mathbf{k}$ is obtained as follows:

$$\frac{d_g}{dt}\mathbf{k} = -\frac{\partial \omega}{\partial \mathbf{x}} = -(\nabla \mathbf{U}) \cdot \mathbf{k}, \tag{9}$$

where the time derivatives are taken along ray paths and $\mathbf{U}$ is a background flow. If we consider the geostrophic flow, we obtain

$$\frac{d_g}{dt}\begin{pmatrix} k \\ l \end{pmatrix} = -\begin{pmatrix} U_x & V_x \\ U_y & V_y \end{pmatrix}\begin{pmatrix} k \\ l \end{pmatrix} \tag{10}$$

and

$$\frac{d_g}{dt}m = -U_z k - V_z l. \tag{11}$$

The horizontal wave vector tends to be infinity at an exponential rate given by the matrix eigenvalues $\sqrt{D}$, where D is the determinant $U_x^2 + V_x U_y$ (here, we assume $U_x + V_y = 0$) and aligns with the direction given by $(-V_x, U_x + \sqrt{D})$. The growing eigenmode is as follows:

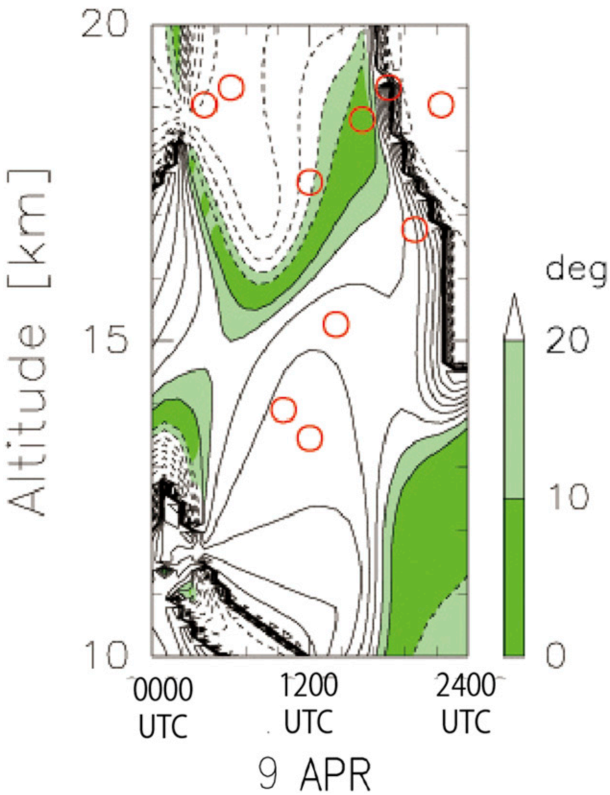

FIG. 12. The time–height section of the angle defined as $\tan^{-1}(\overline{u'w'}/-\overline{v'w'}) \times (180°/\pi)$ during 9 Apr 2013. Contour intervals are 10°. The red circles denote the tropopause at an interval of 1 h.

$$[k(t), l(t)] = (-V_x, U_x + \sqrt{D}) \exp\sqrt{D}t. \qquad (12)$$

Because the intrinsic group velocity decreases with the wavenumber, the packet begins to move with the local background flow, which is called "wave capture" (Bühler and McIntyre 2005).

The evolution of the vertical wavenumber is also given for a large time:

$$m(t) = -\frac{U_z k(t) + V_z l(t)}{\sqrt{D}}, \qquad (13)$$

where $k(t)$ and $l(t)$ correspond to the growing eigenmode. Plougonven and Snyder (2005) found good agreement between the phase lines estimated in this way and the phase lines of the inertia–gravity waves spontaneously generated during the baroclinic wave life cycle.

To elucidate whether gravity waves in the lower stratosphere are captured around the polar front jet, we examined the deformation field of the background wind on 8 and 9 April. Figure 14 shows dw/dz, the direction and intensity of the local deformation of the simulated background wind field $(U_x + \sqrt{D}, V_x)$, and isobars at $z = 10$ km. The background wind is made by using a low-pass filter with a cutoff wavelength of 400 km in the zonal and meridional directions. It is clear that the phase lines tend to align with the dilatation axis around the polar front jet, which is clear in isobars, except for the stationary wave packets that are dominant over the coastal line. Figure 13b shows the longitude–height cross section of dw/dz at 65°S and the slope of the theoretically estimated phase lines of the captured gravity waves. The directions of the predicted phase lines by (12) and (13) are averaged within the rectangles shown in Fig. 13b. It is clear that the phase lines of wave packets around $z = 10$ km are almost parallel to the predicted phase lines, whereas the phase lines in the stratosphere are not. These results suggest that wave packets around $z = 10$ km are captured in the jet streak.

Moreover, the propagation characteristics of the inertia–gravity wave packet around the dynamical tropopause and in the lower stratosphere at 2100 UTC 8 April are examined. From the dispersion relation, the eastward group velocity of a hydrostatic inertia–gravity wave is as follows:

$$C_{gx} = U + \frac{kN^2}{\hat{\omega} m^2}, \qquad (14)$$

where H is the scale height, which is set to 7 km. The wavenumber vectors (k, l, m) are directly estimated from the phase structures shown in Figs. 10, 13, and 14. The intrinsic frequencies and the direction of the wavenumber vector are estimated by the hodograph analyses around the dynamical tropopause and in the lower stratosphere, respectively, as conducted in section 3b.

Around the dynamical tropopause, the horizontal and vertical wavenumbers of the inertia–gravity waves are estimated as about 9.2×10^{-6} and 2.5×10^{-3} m^{-1}. The estimated intrinsic frequency is about 3.3×10^{-4} s^{-1}. The square of the Brunt–Väisälä frequency is about 3.5 $\times 10^{-4}$ s^{-1}. The eastward group velocity of the inertia–gravity waves around the dynamical tropopause is about 11 m s^{-1}, which roughly agrees with the background zonal wind averaged within the rectangles in Fig. 13b (about 13 m s^{-1}). This fact is also consistent with the presumption that the wave-capture mechanism acts on the gravity waves. In the lower stratosphere, the horizontal and vertical wavenumbers of the inertia–gravity waves are estimated as about 2.4×10^{-5} and 2.3×10^{-3} m^{-1}. The estimated intrinsic frequency is about 2.8×10^{-4} s^{-1}. The square of the Brunt–Väisälä frequency is about 4.3×10^{-4} s^{-2}. The eastward group velocity of the inertia–gravity waves in the lower stratosphere is about 3 m s^{-1}, which is largely different from the background zonal wind averaged within the rectangle in Fig. 13b (about 10 m s^{-1}). This fact suggests that the

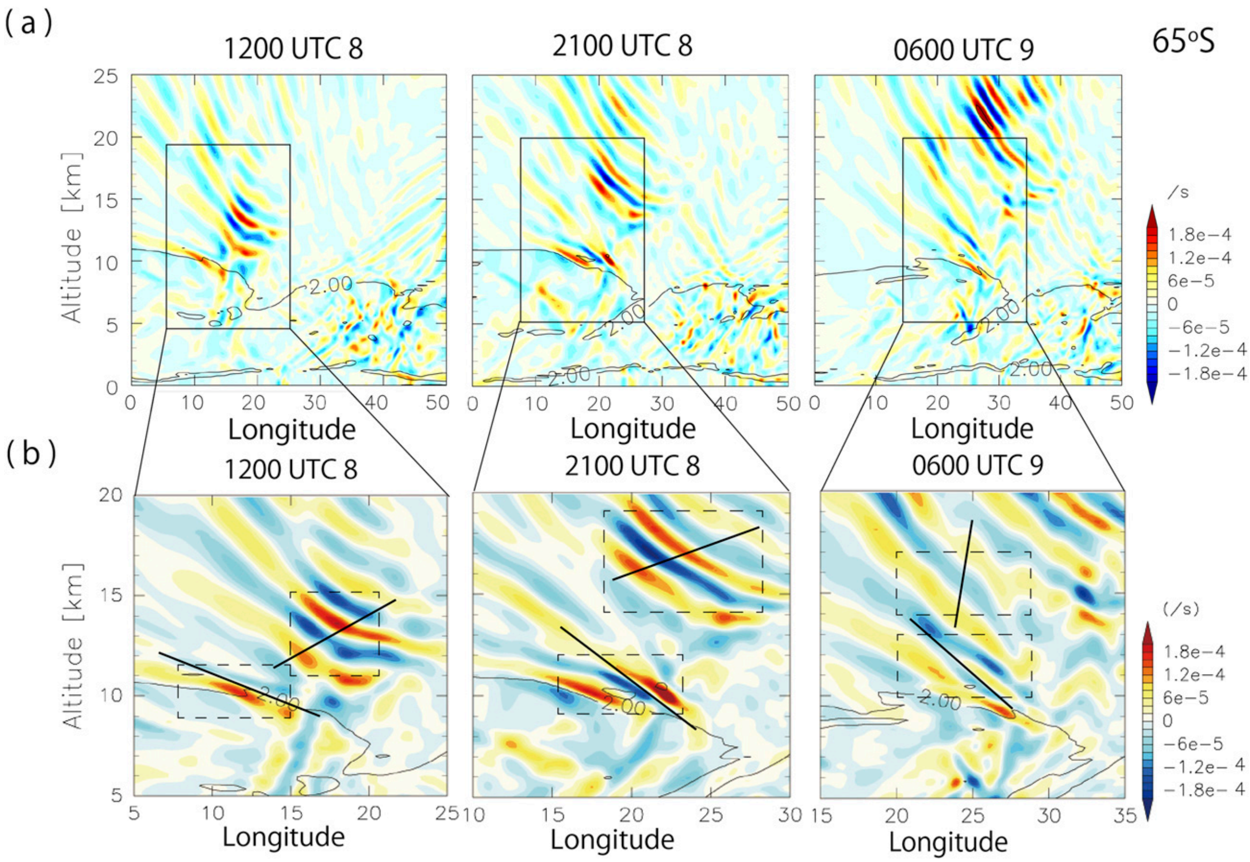

FIG. 13. Snapshots of longitude–height cross sections of vertical divergence of vertical wind components at (a),(b) (left to right) 1200 UTC 8 Apr, 2100 UTC 8 Apr, and 0600 UTC 9 Apr 2013 at 65°S. Black curves denote isolines of 2 PVU. Rectangles in (b) denote the range depicted in (a). The black line segments in (b) show the slopes obtained by the wave capture theory. The slopes are calculated using the background flow averaged within the rectangles.

wave capture mechanism does not act in the lower stratosphere.

d. Gravity wave generation mechanism

Figure 15 shows the latitude–height cross sections of unfiltered dw/dz and meridional winds at 1000 UTC 8 April at 15°E. Strong surface meridional winds are observed around the slope near 73°S in association with the strong anticyclonic anomaly seen in Fig. 7. In Fig. 15a, the wavelike structures over the coast extend continuously from the surface to the lower stratosphere. These features suggest that wave packets observed over the coast near 15°E were generated by the orographic effect there around 1000 UTC 8 April.

A possible generation mechanism for the gravity waves that appeared over the Antarctic ocean is the spontaneous adjustment around the large-scale jet (e.g., O'Sullivan and Dunkerton 1995; Guest et al. 2000; Hertzog et al. 2001; Pavelin et al. 2001; Zhang 2004; Zülicke and Peters 2006; Plougonven and Snyder 2007; Sato and Yoshiki 2008). To explore such a possibility, the horizontal maps of the local Rossby number (Ro) and the residual of the nonlinear balance equation (ΔNBE; Zhang et al. 2001), which are indices showing the degree of flow imbalance, are examined following Sato and Yoshiki (2008). The local Rossby number is defined as the ratio of the absolute value of the relative vorticity ς to the planetary vorticity f ($|\varsigma/f|$) (Pedlosky 1987; Zülicke and Peters 2006; Zülicke and Peters 2008), and ΔNBE is defined as follows:

$$\Delta\mathrm{NBE} = 2J(u, v) + f\varsigma - \alpha\nabla^2 P, \qquad (15)$$

where α and P denote the specific volume and pressure, respectively.

Figures 16a and 16b show maps of ΔNBE and Ro at $z = 8.4$ km at 0600 UTC 8 April. To extract the contamination for these parameters from the gravity waves, we apply a low-pass filter both in the zonal and meridional directions, with a cutoff length of 400 km in advance of the parameter calculations. It is clear that large values are observed in both Ro and ΔNBE fields along the

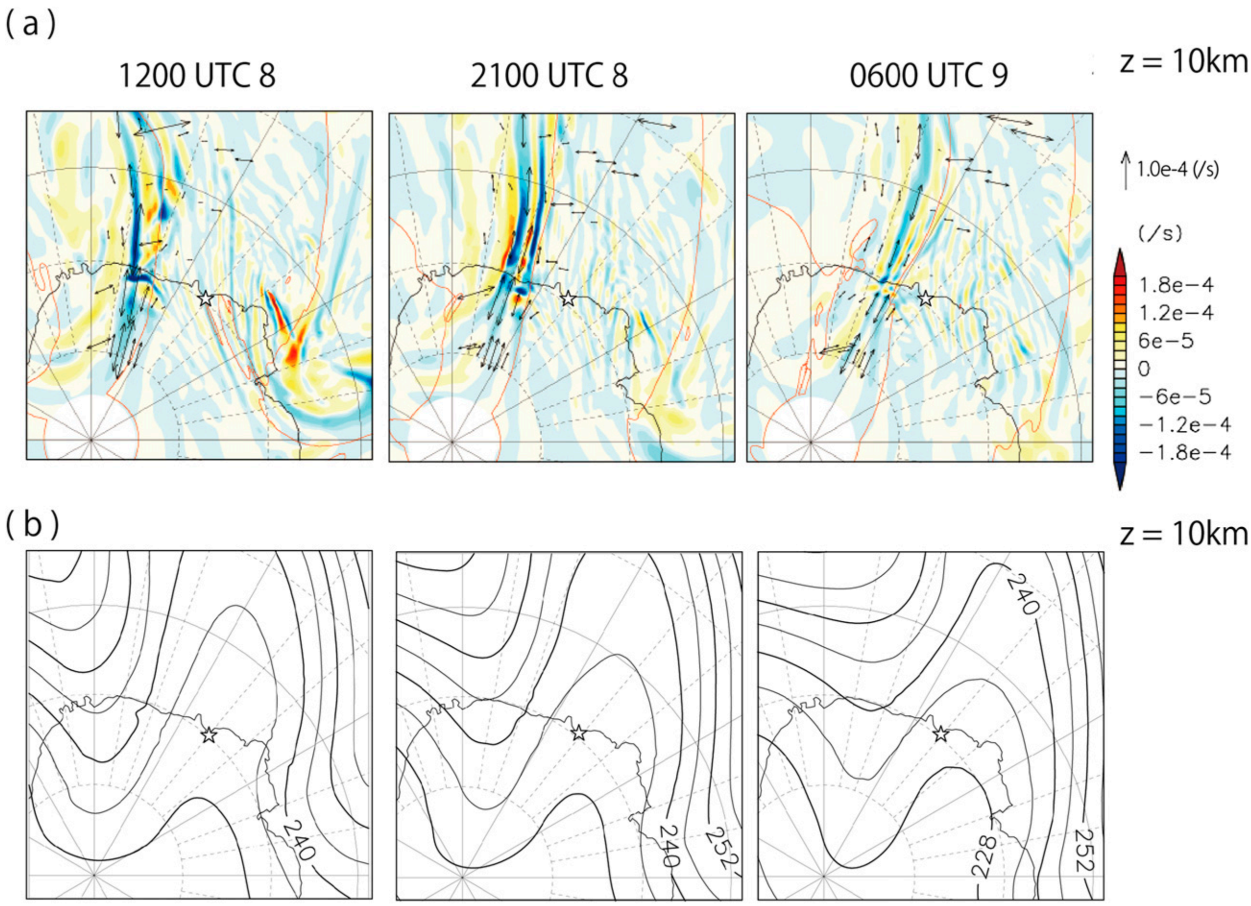

FIG. 14. Snapshots of longitude–height cross sections of dw/dz (color shading) and isobars at (left to right) 1200 UTC 8 Apr, 2100 UTC 8 Apr, and 0600 UTC 9 Apr 2013 at $z = 10$ km. Red curves denote isolines of 2 PVU. Double arrows indicate the orientation (arrows) and intensity (length) of the local deformation. A star denotes the location of Syowa Station (69°S, 39.6°E). The contour interval is 6 hPa.

meandering polar front jet (Fig. 7b). The regions of large Ro and ΔNBE roughly correspond to those where wave packets are dominant over the ocean, as shown in Fig. 11. This feature not only suggests that the polar front jet is unbalanced but also supports the possibility that the gravity waves are generated by spontaneous adjustment around the polar front jet.

5. Discussion

a. *Multiple tropopause structure in the Antarctic atmosphere*

As discussed in sections 3b and 4, the multiple tropopause structure observed at Syowa Station is likely due to inertia–gravity waves. Orographic gravity waves propagate to Syowa Station only around 0600 UTC 9 April (Fig. 11), suggesting that the multiple tropopauses in the time period other than 9 April are caused by nonorographic gravity waves. In addition, even on 9 April, there are only one or two multiple tropopauses in shaded regions where the angle ϑ is less than 20° in Fig. 12. This fact also suggests that the majority of the multiple tropopauses are not due to orographic gravity waves. Thus, in this case, nonorographic gravity waves are mainly responsible for the multiple tropopauses over Syowa Station.

The mechanism of the multiple tropopauses is quite different from those examined in a monsoon region or at midlatitude, in which multiple tropopauses are the true physical boundaries of air masses in the troposphere and stratosphere (e.g., Randel et al. 2007; Pan et al. 2009).

This mechanism enables us to interpret a part of the great seasonal sensitivity of the multiple tropospheres in the polar region: Añel et al. (2008) showed that multiple tropopauses in the polar region tend to occur more often in winter than in summer. The static stability in the polar winter lower stratosphere is particularly weaker than it is in other latitudes (Gettelman et al. 2011). This is likely because ozone heating is absent during the polar night. Based on the radiosonde observations, Yoshiki and Sato (2000) and Tomikawa et al. (2009) also showed that the

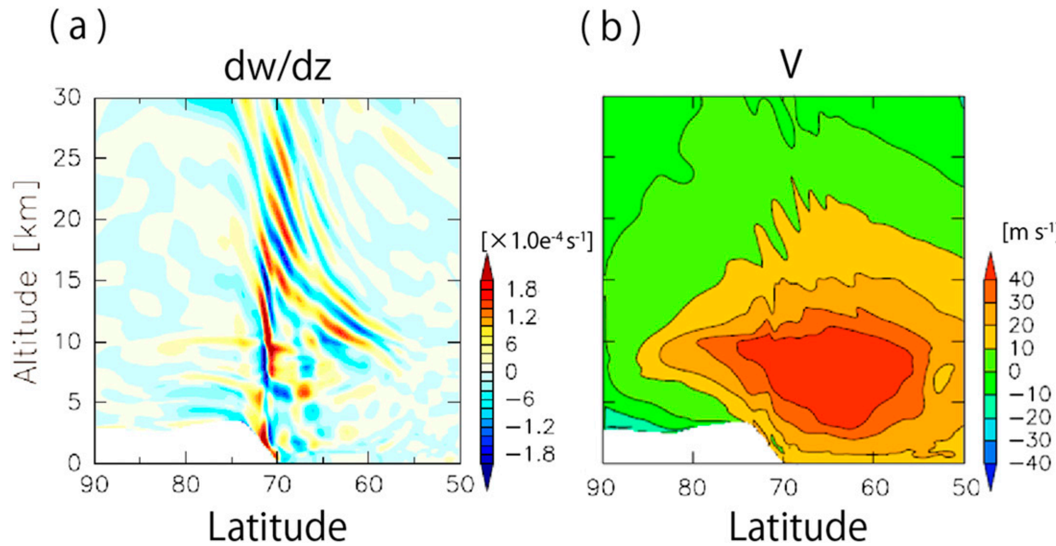

FIG. 15. Snapshot of latitude–height cross sections of (a) vertical divergence of vertical wind components and (b) meridional wind components (contour interval 5 m s^{-1}) at 15°E at 1000 UTC 8 Apr 2013.

static stability in the lower stratosphere over Syowa Station is minimized from April through July. In such a low background static stability in the polar winter lower stratosphere, the temperature fluctuations associated with strong gravity waves have more chances to produce local minima of the static stability. The minima are detected as multiple thermal tropopauses. Moreover, it may be easier to detect multiple tropopause events due to IGWs in the Antarctic winter than in the Arctic, because the static stability in the tropopause inversion layer in the Antarctic in winter is lower than that in the Arctic, partly because of the weaker residual circulation (Birner 2010).

Multiple tropopause structures are often observed when tropopause folding events occur near Syowa Station, as discussed in section 3a. This fact suggests that gravity waves associated with tropopause folding events tend to have large amplitudes. Based on the results shown in section 4, it is inferred that a possible mechanism causing such strong gravity waves is the spontaneous adjustment of flow imbalance. Because the tropopause folding itself is considered to be a part of the baroclinic wave life cycle (e.g., Keyser and Shapiro 1986), drastic tropopause folding events likely accompany strong gravity waves. Such strong baroclinic wave activity around 60°S

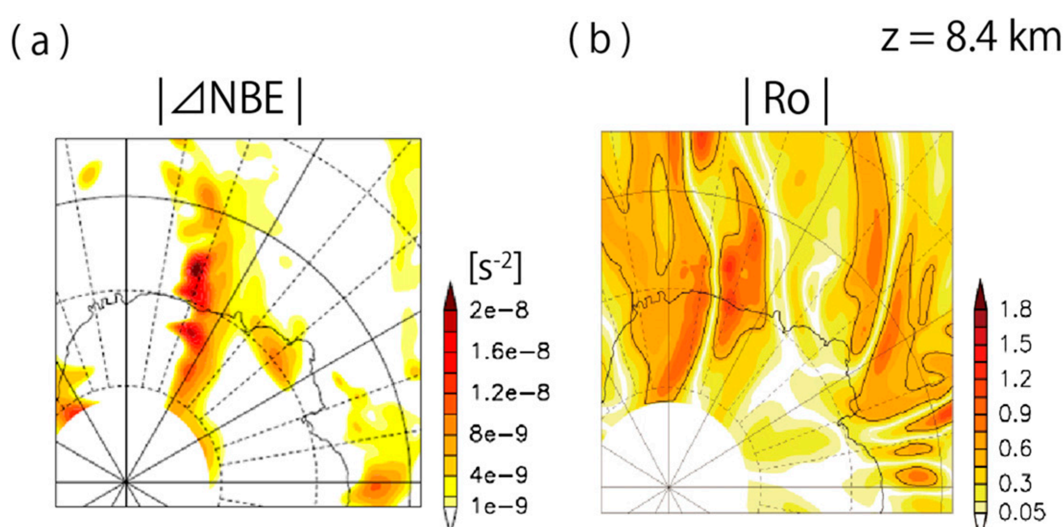

FIG. 16. Snapshots of horizontal maps of (a) ΔNBE and (b) the local Rossby number at $z = 8.4$ km at 0600 UTC 8 Apr 2013.

may be attributed to the strong meridional temperature gradient around 60°S that exists from February to November (Trenberth 1991). In addition, an orographic effect may also be important for a strong gravity wave generation. Generally, the axis of the polar front jet is located along the coast of the Antarctic continent in the polar autumn, as seen from the 2-PVU isolines in Fig. 3. When the polar front jet meanders near Syowa Station, a strong downslope wind toward the ocean occasionally occurs, as in Fig. 15. This may result in the generation of strong gravity waves forming multiple tropopauses.

b. A possible role of inertia–gravity waves appearing in association with tropopause folding events on the mean dynamical field and its seasonal variation

McLandress et al. (2012) discussed the importance of the gravity wave drag (GWD) around 60°S, which is missing in most chemistry–climate models. They showed that extra orographic gravity wave drag at 60°S significantly improved the cold-bias problem and the systematic bias in the timing of final stratospheric warming. They suggested the importance of the effects of both the meridional propagation of gravity waves discussed by Sato et al. (2009) and the vertical propagation of mountain waves excited by isolated mountains on small islands in the Southern Ocean (Alexander et al. 2009). On the other hand, using stratospheric isopycnal balloon observations, Hertzog et al. (2008) showed that the integrated contribution of momentum fluxes by nonorographic gravity waves around 60°S is comparable to that by the orographic gravity waves. Plougonven et al. (2013) intensified this argument using a high-resolution model. Geller et al. (2011) also indicated the enhancement of nonorographic gravity waves at 60°S using the GISS climate model. Although the relative importance of orographically and nonorographically produced gravity waves is an open question for future studies, nonorographic gravity waves around 60°S could contribute to GWDs which may be a key to solve the cold-bias problem.

To quantify the importance of nonorographic gravity waves around 60°S, we examine the magnitude of the absolute momentum fluxes by nonorographic gravity waves generated around 65°S. Geller et al. (2013) estimated the absolute gravity wave momentum fluxes as follows:

$$M^2 = \left(1 - \frac{f^2}{\hat{\omega}^2}\right)\rho_0^2[(\overline{u'w'})^2 + (\overline{v'w'})^2], \tag{16}$$

where

$$\frac{f^2}{\hat{\omega}^2} = \left(\frac{fg}{\overline{T}N^2}\right)^2 \left(\frac{\overline{T'^2}}{\overline{w'^2}}\right). \tag{17}$$

The quantities ρ_0 and $\overline{T}$ are the large-scale density and the temperature, respectively. Here, according to Geller et al. (2013), fluctuations are extracted as a departure from the average over the latitudinal and longitudinal distance of 1000 km.

The absolute momentum flux M is calculated at $z = 20$ km and is averaged over the longitude region of 10°–50°E and the latitude region of 60°–68°S, where nonorographic gravity waves are dominant. To compare the gravity wave drag in this event on the monthly average, we roughly estimate M over the ocean on the basis of two assumptions. First, as estimated from the PANSY and radiosonde observations shown in Fig. 2, the frequency of such an event observed at a fixed point is three times per month. Second, each event continues over 3 days on average. Under these assumptions, the estimated value of M around 65°S in July is 2.2 mPa, which is about 40% of the absolute momentum flux simulated by the gravity wave–resolving high-resolution model, called the Kanto model, which shows realistic distributions of the momentum fluxes associated with the gravity waves and realistic mean fields (Watanabe et al. 2008). It should be noted that the amplitudes of the inertia–gravity waves in NICAM are underestimated compared with the PANSY observation data (e.g., Figs. 6 and 10). Therefore, the momentum fluxes by nonorographic gravity waves are potentially important around 60°S.

6. Summary and future work

The dynamics of the multiple tropopause structure along with the descent of the first tropopause at Syowa Station has been examined by using the PANSY and radiosonde data in combination with numerical simulations using NICAM. Our main results are summarized as follows:

1) The descent of the first tropopause on 7–11 April 2013 was likely due to the passage of a developing tropopause folding. The tropopause folding is located at the eastern edge of a synoptic-scale anticyclone in its breaking stage.
2) Multiple tropopause structures in the lower stratosphere were formed by strong temperature fluctuations associated with inertia–gravity waves having horizontal and vertical wavelengths of about 200 and 3 km, respectively.
3) Gravity waves were likely generated through the spontaneous adjustment from the flow imbalance seen in the meandering polar front jet near the tropopause. Additionally, the orographic gravity wave generation by the steep coast of the Antarctic

Continent in the strong northward downslope wind in front of the strong anticyclone could also be important. It was also indicated that advection by the mean flow perpendicular to the horizontal wavenumber vector is essential for orographic gravity wave propagation.

4) The absolute momentum flux due to nonorographic gravity waves associated with the tropopause folding explains at least 40% of the flux needed for realistic simulation of the polar night jet.

One of the advantages of the present study is its quantitative discussion, which was possible by using both observations and a numerical model with high resolution. Statistical studies are needed to confirm our results, with many case studies using observations and numerical simulations. Moreover, it would be interesting to investigate the quantification of the STE associated with IGWs (Danielsen et al. 1991) under the low static stability around the tropopause in the polar winter. Sato et al. (2014) showed that a multiple tropopause structure is most frequent during the polar winter season. Further studies are needed to examine the dynamics of the multiple tropopauses in various seasons.

Acknowledgments. The authors thank associate professors H. Miura and M. Koike for their many useful comments and discussions. Numerical simulations were run on the supercomputer in NIPR. All figures in this paper are pictured by using Dennou Club Library (DCL). This work was supported by the program for Leading Graduate Schools, MEXT, Japan. This study was also supported by Grant-in-Aid Scientific Research (A) 25247075 and by Grant-in-Aid for Research Fellow (26-9257) provided by the Japan Society for the Promotion of Science (JSPS).

REFERENCES

Alexander, M. J., S. D. Eckermann, D. Broutman, and J. Ma, 2009: Momentum flux estimates for South Georgia Island mountain waves in the stratosphere observed via satellite. *Geophys. Res. Lett.,* **36,** L12816, doi:10.1029/2009GL038587.

Añel, J. A., J. C. Antuña, L. de la Torre, J. M. Castanheira, and L. Gimeno, 2008: Climatological features of global multiple tropopause events. *J. Geophys. Res.,* **113,** D00B08, doi:10.1029/2007JD009697.

Beres, J. H., M. J. Alexander, and J. R. Holton, 2004: A method of specifying the gravity wave spectrum above convection based on latent heating properties and background wind. *J. Atmos. Sci.,* **61,** 324–337, doi:10.1175/1520-0469(2004)061<0324:AMOSTG>2.0.CO;2.

Berthet, G., J. G. Esler, and P. H. Haynes, 2007: A Lagrangian perspective of the tropopause and the ventilation of the lowermost stratosphere. *J. Geophys. Res.,* **112,** D18102, doi:10.1029/2006JD008295.

Birner, T., 2010: Residual circulation and tropopause structure. *J. Atmos. Sci.,* **67,** 2582–2600, doi:10.1175/2010JAS3287.1.

Bühler, O., and M. E. McIntyre, 2005: Wave capture and wave–vortex duality. *J. Fluid Mech.,* **534,** 67–95, doi:10.1017/S0022112005004374.

Danielsen, E. F., R. S. Hipskind, W. L. Starr, J. F. Vedder, S. E. Gaines, D. Kley, and K. K. Kelly, 1991: Irreversible transport in the stratosphere by internal waves of short vertical wavelength. *J. Geophys. Res.,* **96,** 17 433–17 452, doi:10.1029/91JD01362.

Dee, D. P., and Coauthors, 2011: The ERA-Interim reanalysis: Configuration and performance of the data assimilation system. *Quart. J. Roy. Meteor. Soc.,* **137,** 553–597, doi:10.1002/qj.828.

Eckermann, S. D., and W. K. Hocking, 1989: Effect of superposition on measurements of atmospheric gravity waves: A cautionary note and some reinterpretations. *J. Geophys. Res.,* **94,** 6333–6339, doi:10.1029/88JD03916.

Eyring, V., T. G. Shepherd, and D. W. Waugh, Eds., 2010: SPARC CCMVal report on the evaluation of chemistry–climate models. SPARC Tech. Rep. 5, WCRP-132, WMO/TD-1526, 434 pp. [Available online at http://www.atmosp.physics.utoronto.ca/SPARC/ccmval_final/.]

Gal-Chen, T., and R. Somerville, 1975: On the use of a coordinate transformation for the solution of the Navier–Stokes equations. *J. Comput. Phys.,* **17,** 209–228, doi:10.1016/0021-9991(75)90037-6.

Geller, M. A., and Coauthors, 2011: New gravity wave treatments for GISS climate models. *J. Climate,* **24,** 3989–4002, doi:10.1175/2011JCLI4013.1.

——, and Coauthors, 2013: A comparison between gravity wave momentum fluxes in observations and climate models. *J. Climate,* **26,** 6383–6405, doi:10.1175/JCLI-D-12-00545.1.

Gettelman, A., P. Hoor, L. L. Pan, W. J. Randel, M. I. Hegglin, and T. Birner, 2011: The extratropical upper troposphere and lower stratosphere. *Rev. Geophys.,* **49,** RG3003, doi:10.1029/2011RG000355.

Guest, F., M. Reeder, C. Marks, and D. Karoly, 2000: Inertia–gravity waves observed in the lower stratosphere over Macquarie Island. *J. Atmos. Sci.,* **57,** 737–752, doi:10.1175/1520-0469(2000)057<0737:IGWOIT>2.0.CO;2.

Haynes, P. H., and E. Shuckburgh, 2000: Effective diffusivity as a diagnostic of atmospheric transport: 2. Troposphere and lower stratosphere. *J. Geophys. Res.,* **105,** 22 795–22 810, doi:10.1029/2000JD900092.

Hertzog, A., C. Souprayen, and A. Hauchecorne, 2001: Observation and backward trajectory of an inertio–gravity wave in the lower stratosphere. *Ann. Geophys.,* **19,** 1141–1155, doi:10.5194/angeo-19-1141-2001.

——, G. Boccara, R. A. Vincent, F. Vial, and P. Cocquerez, 2008: Estimation of gravity wave momentum flux and phase speeds from quasi-Lagrangian stratospheric balloon flights. Part II: Results from the Vorcore campaign in Antarctica. *J. Atmos. Sci.,* **65,** 3056–3070, doi:10.1175/2008JAS2710.1.

Hoskins, B. J., M. E. McIntyre, and A. W. Robertson, 1985: On the use and significance of isentropic potential vorticity maps. *Quart. J. Roy. Meteor. Soc.,* **111,** 877–946, doi:10.1002/qj.49711147002.

Keyser, D. A., and M. A. Shapiro, 1986: A review of the structure and dynamics of upper-level frontal zones. *Mon. Wea. Rev.,* **114,** 452–499, doi:10.1175/1520-0493(1986)114<0452:AROTSA>2.0.CO;2.

Klemp, J. B., 2011: A terrain-following coordinate with smoothed coordinate surfaces. *Mon. Wea. Rev.,* **139,** 2163–2169, doi:10.1175/MWR-D-10-05046.1.

Koch, S. E., and Coauthors, 2005: Turbulence and gravity waves within an upper-level front. *J. Atmos. Sci.,* **62,** 3885–3908, doi:10.1175/JAS3574.1.

Kohma, M., and K. Sato, 2011: The effects of atmospheric waves on the amounts of polar stratospheric clouds. *Atmos. Chem. Phys.,* **11,** 11 535–11 552, doi:10.5194/acp-11-11535-2011.

Lamarque, J.-F., A. O. Langford, and M. H. Proffitt, 1996: Cross-tropopause mixing of ozone through gravity wave breaking: Observation and modeling. *J. Geophys. Res.,* **101,** 22 969–22 976, doi:10.1029/96JD02442.

McLandress, C., T. G. Shepherd, S. Polavarapu, and S. R. Beagley, 2012: Is missing orographic gravity wave drag near 60°S the cause of the stratospheric zonal wind biases in chemistry–climate models? *J. Atmos. Sci.,* **69,** 802–818, doi:10.1175/JAS-D-11-0159.1.

Miura, H., M. Satoh, T. Nasuno, A. T. Noda, and K. Oouchi, 2007: A Madden–Julian Oscillation event simulated by a global cloud-resolving model. *Science,* **318,** 1763–1765, doi:10.1126/science.1148443.

Nakanishi, M., and H. Niino, 2004: An improved Mellor–Yamada Level-3 model with condensation physics: Its design and verification. *Bound.-Layer Meteor.,* **112,** 1–31, doi:10.1023/B:BOUN.0000020164.04146.98.

Olsen, M. A., A. R. Douglass, P. A. Newman, J. C. Gille, B. Nardi, V. A. Yudin, and R. Khosravi, 2008: HIRDLS observations and simulation of a lower stratospheric intrusion of tropical air to high latitudes. *Geophys. Res. Lett.,* **35,** L21813, doi:10.1029/2008GL035514.

——, ——, M. R. Schoeberl, J. M. Rodriquez, and Y. Yoshida, 2010: Interannual variability of ozone in the winter lower stratosphere and the relationship to lamina and irreversible transport. *J. Geophys. Res.,* **115,** D15305, doi:10.1029/2009JD013004.

O'Sullivan, D. J., and T. J. Dunkerton, 1995: Generation of inertia–gravity waves in a simulated life cycle of baroclinic instability. *J. Atmos. Sci.,* **52,** 3695–3716, doi:10.1175/1520-0469(1995)052<3695:GOIWIA>2.0.CO;2.

Pan, L. L., and Coauthors, 2009: Tropospheric intrusions associated with the secondary tropopause. *J. Geophys. Res.,* **114,** D10302, doi:10.1029/2008JD011374.

Pavelin, E., J. Whiteway, and G. Vaughan, 2001: Observation of gravity wave generation and breaking in the lowermost stratosphere. *J. Geophys. Res.,* **106,** 5173–5179, doi:10.1029/2000JD900480.

Pedlosky, J., 1987: *Geophysical Fluid Dynamics.* 2nd ed. Springer, 128 pp.

Peevey, T. R., J. C. Gille, C. R. Homeyer, and G. L. Manney, 2014: The double tropopause and its dynamical relationship to the tropopause inversion layer in storm track regions. *J. Geophys. Res. Atmos.,* **119,** 10 194–10 212, doi:10.1002/2014JD021808.

Plougonven, R., and C. Snyder, 2005: Gravity waves excited by jets: Propagation versus generation. *Geophys. Res. Lett.,* **32,** L18802, doi:10.1029/2005GL023730.

——, and ——, 2007: Inertia–gravity waves spontaneously generated by jets and fronts. Part I: Different baroclinic life cycles. *J. Atmos. Sci.,* **64,** 2502–2520, doi:10.1175/JAS3953.1.

——, A. Hertzog, and L. Guez, 2013: Gravity waves over Antarctica and the Southern Ocean: Consistent momentum fluxes in mesoscale simulations and stratospheric balloon observations. *Quart. J. Roy. Meteor. Soc.,* **139,** 101–118, doi:10.1002/qj.1965.

Randel, W. J., D. J. Seidel, and L. L. Pan, 2007: Observational characteristics of double tropopauses. *J. Geophys. Res.,* **112,** D07309, doi:10.1029/2006JD007904.

Rao, T. N., J. Arvelius, and S. Kirkwood, 2008: Climatology of tropopause folds over a European Arctic station (Esrange). *J. Geophys. Res.,* **113,** D00B03, doi:10.1029/2007JD009638.

Richter, J. H., F. Sassi, and R. R. Garcia, 2010: Toward a physically based gravity wave source parameterization in a general circulation model. *J. Atmos. Sci.,* **67,** 136–156, doi:10.1175/2009JAS3112.1.

Sato, K., and M. Yamada, 1994: Vertical structure of atmospheric gravity waves revealed by the wavelet analysis. *J. Geophys. Res.,* **99,** 20 623–20 631, doi:10.1029/94JD01818.

——, and M. Yoshiki, 2008: Gravity wave generation around the polar vortex in the stratosphere revealed by 3-hourly radiosonde observations at Syowa Station. *J. Atmos. Sci.,* **65,** 3719–3735, doi:10.1175/2008JAS2539.1.

——, D. J. O'Sullivan, and T. J. Dunkerton, 1997: Low-frequency inertia-gravity waves in the stratosphere revealed by three-week continuous observation with the MU radar. *Geophys. Res. Lett.,* **24,** 1739–1742.

——, S. Watanabe, Y. Kawatani, Y. Tomikawa, K. Miyazaki, and M. Takahashi, 2009: On the origins of mesospheric gravity waves. *Geophys. Res. Lett.,* **36,** L19801, doi:10.1029/2009GL039908.

——, S. Tateno, S. Watanabe, and Y. Kawatani, 2012: Gravity wave characteristics in the Southern Hemisphere revealed by a high-resolution middle-atmosphere general circulation model. *J. Atmos. Sci.,* **69,** 1378–1396, doi:10.1175/JAS-D-11-0101.1.

——, and Coauthors, 2014: Program of the Antarctic Syowa MST/IS Radar (PANSY). *J. Atmos. Sol.-Terr. Phys.,* **118,** 2–15, doi:10.1016/j.jastp.2013.08.022.

Satoh, M., T. Matsuno, H. Tomita, H. Miura, T. Nasuno, and S. Iga, 2008: Nonhydrostatic icosahedral atmospheric model (NICAM) for global cloud resolving simulations. *J. Comput. Phys.,* **227,** 3486–3514, doi:10.1016/j.jcp.2007.02.006.

Schär, C., D. Leuenberger, O. Fuhrer, D. Lüthi, and C. Girard, 2002: A new terrain-following vertical coordinate formulation for atmospheric prediction models. *Mon. Wea. Rev.,* **130,** 2459–2480, doi:10.1175/1520-0493(2002)130<2459:ANTFVC>2.0.CO;2.

Schmidt, T., G. Beyerle, S. Heise, J. Wickert, and M. Rothacher, 2006: A climatology of multiple tropopauses derived from GPS radio occultations with CHAMP and SAC-C. *Geophys. Res. Lett.,* **33,** L04808, doi:10.1029/2005GL024600.

Scinocca, J. F., 2003: An accurate spectral nonorographic gravity wave drag parameterization for general circulation models. *J. Atmos. Sci.,* **60,** 667–682, doi:10.1175/1520-0469(2003)060<0667:AASNGW>2.0.CO;2.

Shibata, T., K. Sato, H. Kobayashi, M. Yabuki, and M. Shiobara, 2003: Antarctic polar stratospheric clouds under temperature perturbation by nonorogaphic inertia gravity waves observed by micropulse lidar at Syowa Station. *J. Geophys. Res.,* **108,** 4105, doi:10.1029/2002JD002713.

Stolarski, R. S., A. R. Douglass, M. Gupta, P. A. Newman, S. Pawson, M. R. Schoeberl, and J. E. Nielsen, 2006: An ozone increase in the Antarctic summer stratosphere: A dynamical response to the ozone hole. *Geophys. Res. Lett.,* **33,** L21805, doi:10.1029/2006GL026820.

Tomikawa, Y., Y. Nishimura, and T. Yamanouchi, 2009: Characteristics of tropopause and tropopause inversion layer in the polar region. *SOLA,* **5,** 141–144, doi:10.2151/sola.2009-036.

Tomita, H., H. Miura, S. Iga, T. Nasuno, and M. Satoh, 2005: A global could-resolving simulation: Preliminary results from an aqua planet experiment. *Geophys. Res. Lett.,* **32,** L08805, doi:10.1029/2005GL022459.

Trenberth, K. E., 1991: Storm tracks in the Southern Hemisphere. *J. Atmos. Sci.,* **48,** 2159–2178, doi:10.1175/1520-0469(1991)048<2159:STITSH>2.0.CO;2.

Vaughan, G., and R. M. Worthington, 2007: Inertia–gravity waves observed by the UK MST radar. *Quart. J. Roy. Meteor. Soc.,* **133,** 179–188, doi:10.1002/qj.142.

Vincent, R. A., and I. M. Reid, 1983: HF Doppler measurements of mesospheric gravity wave momentum fluxes. *J. Atmos. Sci.,* **40,** 1321–1333, doi:10.1175/1520-0469(1983)040<1321:HDMOMG>2.0.CO;2.

Vogel, B., and Coauthors, 2011: Transport pathways and signatures of mixing in the extratropical tropopause region derived from Lagrangian model simulations. *J. Geophys. Res.,* **116,** D05306, doi:10.1029/2010JD014876.

Watanabe, S., Y. Kawatani, Y. Tomikawa, K. Miyazaki, M. Takahashi, and K. Sato, 2008: General aspects of a T213L256 middle atmosphere general circulation model. *J. Geophys. Res.,* **113,** D12110, doi:10.1029/2008JD010026.

Wilcox, L. J., B. J. Hoskins, and K. P. Shine, 2012: A global blended tropopause based on ERA data. Part I: Climatology. *Quart. J. Roy. Meteor. Soc.,* **138,** 561–575, doi:10.1002/qj.951.

WMO, 1957: Meteorology—A three-dimensional science. *WMO Bull.,* **6,** 134–138.

Yoshiki, M., and K. Sato, 2000: A statistical study of gravity waves in the polar regions based on operational radiosonde data. *J. Geophys. Res.,* **105,** 17 995–18 011, doi:10.1029/2000JD900204.

Zhang, F., 2004: Generation of mesoscale gravity waves in upper-tropospheric jet–front systems. *J. Atmos. Sci.,* **61,** 440–457, doi:10.1175/1520-0469(2004)061<0440:GOMGWI>2.0.CO;2.

——, C. A. Davis, M. L. Kaplan, and S. E. Koch, 2001: Wavelet analysis and the governing dynamics of a large-amplitude mesoscale gravity-wave event along the East Coast of the United States. *Quart. J. Roy. Meteor. Soc.,* **127,** 2209–2245, doi:10.1002/qj.49712757702.

Zülicke, C., and D. Peters, 2006: Simulation of inertia–gravity waves in a poleward-breaking Rossby wave. *J. Atmos. Sci.,* **63,** 3253–3276, doi:10.1175/JAS3805.1.

——, and ——, 2008: Parameterization of strong stratospheric inertia–gravity waves forced by poleward-breaking Rossby waves. *Mon. Wea. Rev.,* **136,** 98–119, doi:10.1175/2007MWR2060.1.